



저작자표시-비영리-변경금지 2.0 대한민국

이용자는 아래의 조건을 따르는 경우에 한하여 자유롭게

- 이 저작물을 복제, 배포, 전송, 전시, 공연 및 방송할 수 있습니다.

다음과 같은 조건을 따라야 합니다:



저작자표시. 귀하는 원저작자를 표시하여야 합니다.



비영리. 귀하는 이 저작물을 영리 목적으로 이용할 수 없습니다.



변경금지. 귀하는 이 저작물을 개작, 변형 또는 가공할 수 없습니다.

- 귀하는, 이 저작물의 재이용이나 배포의 경우, 이 저작물에 적용된 이용허락조건을 명확하게 나타내어야 합니다.
- 저작권자로부터 별도의 허가를 받으면 이러한 조건들은 적용되지 않습니다.

저작권법에 따른 이용자의 권리는 위의 내용에 의하여 영향을 받지 않습니다.

이것은 [이용허락규약\(Legal Code\)](#)을 이해하기 쉽게 요약한 것입니다.

[Disclaimer](#)

공학박사 학위논문

**Surface Damage Mechanism of Tungsten
by Heat Flux and Deuterium Ion Irradiation
in Nuclear Fusion**

핵융합 열 속 및 중수소 이온 조사에 의한
텅스텐 표면 손상 거동 연구

2015년 2월

서울대학교 대학원

에너지시스템 공학부

김 현 수

**Surface Damage Mechanism of Tungsten
by Heat Flux and Deuterium Ion Irradiation
in Nuclear Fusion**

핵융합 열 속 및 중수소 이온 조사에 의한
텅스텐 표면 손상 거동 연구

지도 교수 김 곤 호

이 논문을 공학박사 학위논문으로 제출함
2014년 12월

서울대학교 대학원
에너지시스템공학부
김 현 수

김현수의 박사 학위논문을 인준함
2014년 12월

위 원 장 _____ 황 용 석 _____ (인)

부위원장 _____ 김 곤 호 _____ (인)

위 원 _____ 백 경 호 _____ (인)

위 원 _____ 한 흥 남 _____ (인)

위 원 _____ 최 수 석 _____ (인)

Abstract

Surface Damage Mechanism of Tungsten by Heat Flux and Deuterium Ion Irradiation in Nuclear Fusion

Hyun-Su Kim

Department of Energy System Engineering

The Graduated School

Seoul National University

Tungsten is a very promising material for use as a plasma-facing component in high-power fusion plasma devices, because of its high thermal conductivity, melting point, and plasma resistance. However, even tungsten is not fully capable of withstanding the energy transferred from the core plasma. In such a situation, the tungsten surface becomes damaged and develops both morphological and structural variations under specific plasma conditions. For plasma-facing material, energy transfer from the plasma to the material surface causes surface damage through thermal-dominant and particle-dominant effects. Each effect manifests on the tungsten surface in different ways, causing various types of damage. In addition, this damage manifests differently under the same plasma conditions, depending on the characteristics of the facing material. Therefore, an understanding of the damage sustained on the tungsten surface is required, considering both the correlation between thermal/particle effects from the plasma and the characteristics of the facing material.

In this dissertation, this damage generation is studied using the heat flux and deuterium-ion irradiation of tungsten targets having vertically and horizontally elongated grains. The heat-flux irradiation is conducted with heat-flux conditions of 5 MW/m² and a surface temperature of 1,700 °C, and the deuterium-ion irradiation is conducted with ion fluence conditions of 8.3×10^{23} – 1.9×10^{25} m⁻² and an incident energy of 50–200 eV.

Heat-flux irradiation causes a tungsten target to recrystallize with increased grain size and saturated recrystallized-layer thickness. Differences in the initial grain structures of various tungsten targets lead to differences in the recrystallized targets, which initially have vertical or horizontal grain elongations. Only a recrystallized tungsten target that has vertically elongated initial grains demonstrates a large amount of sub-grains and internal cracks generated at the sub-grain boundaries. In contrast, a tungsten target with horizontally elongated grains exhibits no internal damage, e.g., crack and bubble structures.

After deuterium-ion irradiation, a specific structure called a blister is generated on the tungsten target surface. Depending on their sizes and shapes, the blisters are classified as being small dome-shaped, medium terrace-shaped, and large irregular-shaped. The small dome-shaped blister has the thinnest roof and an inclined side wall, while the medium terrace-shaped and large irregular-shaped blisters originate from near-surface grain boundaries and have thicker roofs than those of the small blisters. On the surface of a small dome-shaped blister, the side wall is exposed to the deuterium-ion flux at an angle of 70°, which is the optimum value for maximum sputtering. The small dome-shaped blister is eradicated from the side wall by an increased sputtering-aided burst. The burst area is expanded along the blister edge,

satisfying the required angle condition. In the case of a medium terrace-shaped blister, the blister is also destroyed through a local sputtering increment at the inclined side wall of the blister. However, an increase in the sputtering incident angle is not effective in the case of the large irregular-shaped blister, because of its moderately swollen surface. From these results, it is apparent that the small dome-shaped blister has the greatest susceptibility to the effects of high-energy deuterium ions. Thus, a vertically elongated grain structure that has a large number of small blisters only is strongly affected by deuterium-ion irradiation.

The tungsten surfaces damaged by heat flux and deuterium-ion irradiation are aggravated using additional ion and heat-flux irradiation, respectively. The deuterium-ion irradiation causes sub-grain ejection with very little frequency from pre-heat-flux-irradiated tungsten with a vertically elongated grain. In contrast, hole structures are frequently generated on pre-recrystallized tungsten with a horizontally elongated grain. Additional heat-flux irradiation causes all three kinds of blisters to be aggravated by the thermal bursting due to this additional irradiation. The small dome-shaped blisters are fully destroyed, while the medium terrace-shaped and large irregular-shaped blisters increase in size and are partially destroyed but retain their size and shape.

Keywords: Plasma surface interaction, high heat flux, particle flux, tungsten, recrystallization, blister

Student Number: 2008-30273

Contents

Abstract	i
Contents	iv
List of Tables	viii
List of Figures	ix
Chapter 1 Introduction	1
1.1 Tungsten facing with fusion plasma	1
1.2 Energy transfer to wall material in fusion devices.....	4
1.2.1 Energy transfer by heat flux	5
1.2.2 Particle flux irradiation	8
1.3 Local damages of tungsten in fusion plasma.....	10
1.4 Objectives	12

Chapter 2 Experimental Setup..... 1 4

2.1 Heat flux irradiation facility	1 4
2.1.1 High power thermal plasma torch.....	1 4
2.1.2 Target holder	1 8
2.1.3 Temperature measurement	2 0
2.1.4 Heat flux measurement.....	2 2
2.1.5 Operating Characteristics	2 5
2.2 Ion flux irradiation facility.....	3 1
2.2.1 Electron cyclotron resonance plasma generator	3 1
2.2.2 Target holder	3 3
2.2.3 Deuterium-ion flux characteristics	3 3
2.3 Target materials	3 6
2.3.1 Tungsten target type.....	3 6
2.3.2 Surface finishing method.....	4 0

Chapter 3 Thermal-Driven Target surface damages 4 3

3.1 Characteristics of recrystallized target surface.....	4 3
3.1.1 Tungsten target recrystallization.....	4 3
3.1.2 Recrystallized grain characteristics under various heat-flux irradiation conditions.....	4 6
3.2 Recrystallization characteristics of different tungsten types.....	5 1
3.3 Defects rearrangement during the recrystallization.....	5 3

Chapter 4 Particle-Driven Target Surface Damage 5 5

4.1 Blister generation on different tungsten target types	5 5
4.2 Characteristics of small blisters on the target with vertically elongated grain.....	5 9
4.2.1 Small dome-shaped blister generation.....	5 9
4.2.2 Characteristics of small dome-shaped blister with irradiation conditions	6 3
4.3 Characteristics of medium terrace-shaped and large irregular-shaped blisters on the target surface with horizontally elongated grain.....	7 0
4.3.1 Generation of medium and large blisters.....	7 0
4.3.2 Characteristics of medium and large blisters depending on irradiation conditions.....	7 5
4.4 Destruction of blisters by sputtering aided bursting	8 1
4.4.1 Small dome-shaped blister destruction mechanism	8 1
4.4.2 Destruction of medium terrace-shaped blisters.....	8 5

Chapter 5 Aggravation of pre-generated damage on tungsten surface by additional thermal and particle flux	8 8
5.1 Thermally pre-irradiated tungsten damage aggravation by deuterium-ion irradiation.....	8 8
5.1.1 Ion flux irradiation on recrystallized tungsten.....	8 8
5.1.2 Characteristics of aggravated damage of thermally pre-irradiated tungsten by ion irradiation.....	8 9
5.2 Damage aggravation of ion pre-irradiated tungsten by heat flux irradiation.....	9 8
5.2.1 Heat-flux irradiation on blister reach surface of tungsten.....	9 8
5.2.2 Characteristics of aggravated damage of ion pre-irradiated tungsten by heat-flux irradiation.....	9 9
Chapter 6 Conclusion	1 0 4
Bibliography.....	1 0 9
초 록	1 1 9

List of Tables

Table 1.1	Characteristics of tungsten.....	3
Table 1.2	Advantages and disadvantages of tungsten.....	4
Table 2.1	Ion irradiation conditions	3 4
Table 2.2	Characteristics of tungsten targets.	3 7
Table 2.3	Grinding and polishing conditions for tungsten target finishing.....	4 1
Table 4.1	Classification of blisters generated by deuterium ion irradiation.....	5 6
Table 5.1	Conditions of pre-heat flux irradiation and aggravation by deuterium ion irradiation.....	8 9
Table 5.2	Conditions of pre-ion irradiation and aggravation by heat flux irradiation	9 8

List of Figures

Figure 1.1	Overview of the power densities and durations of different events in ITER	9
Figure 2.1	Design of hollow electrode thermal plasma torch.....	1 6
Figure 2.2	Schematic diagram of substrate holder	1 9
Figure 2.3	Design of substrate holder.....	1 9
Figure 2.4	(a) Schematic diagram of surface temperature measurement and (b) flow chart of temperature calculation in pyrometer	2 1
Figure 2.5	Schematic diagram of heat flux measurements by (a) calorimetry of coolant and (b) heat transfer in disk.....	2 4
Figure 2.6	Schematic diagram of heat flux irradiation facility	2 6
Figure 2.7	Picture of heat flux irradiation facility.....	2 7
Figure 2.8	Operating sequence of heat flux irradiations using hollow electrode thermal plasma torch.....	2 9
Figure 2.9	Variation of thermal loads according to substrate position.....	3 0
Figure 2.10	Variation of surface temperature according to substrate position.....	3 0
Figure 2.11	Schematic diagram of deuterium ion irradiation facility	3 2
Figure 2.12	Schematic diagram of the target holder for deuterium ion irradiation	3 5
Figure 2.13	Schematic diagram of the basic powder metallurgical production process of tungsten	3 8
Figure 2.14	Grain orientation map and grain boundary misorientation angle distributions of (a) vertically elongated W – KW-v, (b) horizontally elongated W – PW-h and (c) horizontally elongated W – KW-h	3 9

Figure 3.1	Change of Grain Structure by Heat Flux Irradiation (a)Surface SEM image and (b) EBSD analysis results of as received PW-h target (c) Surface SEM image and (d) EBSD analysis results of recrystallized PW-h with 1699 °C, 200 s and 4.1 MW/m ² (828 MJ/m ²).....	4 4
Figure 3.2	Thermal grooving of grain boundary in recrystallized PW-h target with conditions of T = 1703 °C, 400 s, 5.9 MW/m ² (2360 MJ/m ²).....	4 5
Figure 3.3	Grain size variation according to heat flux irradiation time	4 8
Figure 3.4	Thickness variations of recrystallized layer according to the heat flux irradiation time	
	(a) 180 s, T = 1758 °C with 1157 MJ/m ² (6.4 MW/m ²)	
	(b) 300 s, T = 1825 °C with 1729 MJ/m ² (5.8 MW/m ²)	
	(c) 420 s, T = 1791 °C with 2496 MJ/m ² (5.9 MW/m ²).....	4 9
Figure 3.5	Recrystallization thickness according to heat flux irradiation time.....	5 0
Figure 3.6	Grain Structure Change of Different Tungsten Type	
	(a) PW-h heat flux irradiated in 1699 °C, 200 s and 4.1 MW/m ² (828 MJ/m ²) (b)KW-v heat flux irradiated in = 1615 °C, 200 s and 4.3 MW/m ² (872 MJ/m ²).....	5 2
Figure 3.7	Inside damages of different type W during Recrystallization	
	(a) PW-h heat flux irradiated in 1690 °C, 200 s	
	(b) KW-v heat flux irradiated in = 1697 °C, 400 s.....	5 4
Figure 4.1	SEM image of blisters on surface of deuterium ion irradiated	
	(a) KW-v and (b) PW-h targets	5 7
Figure 4.2	Cross sectional SEM images of (a) small blister on ion irradiated KW-v and (b) medium and large blisters on ion irradiated PW-h.....	5 8

Figure 4.3	Blister generation by ion flux irradiation with conditions of 100 eV and $1.66 \times 10^{24} \text{ m}^{-2}$ (10 min)	6 1
Figure 4.4	Generation characteristics of small blister with conditions of 100 eV and $8.30 \times 10^{23} \text{ m}^{-2}$ (5 min).....	6 1
Figure 4.5	Sequential diagram of small dome-shaped blister generation by deuterium ion irradiation.....	6 2
Figure 4.6	Cross sectional SEM image of small dome-shaped blister	6 2
Figure 4.7	Character of small blister according to increment of ion fluence.....	6 5
Figure 4.8	Size and number density of small blister according to ion fluence.....	6 7
Figure 4.9	Character of small blister according to ion energy	6 8
Figure 4.10	Size and number density of small blister according to ion fluence.....	6 9
Figure 4.11	Medium terrace-shaped and large irregular-shaped blisters on the deuterium ion irradiated tungsten target with horizontally elongated grains	7 2
Figure 4.12	Cross sectional SEM images of (a) medium terrace-shaped blister, (b) and (c) large irregular-shaped blister	7 3
Figure 4.13	Schematic diagram of (a) medium terrace-shaped blister generation (b) large irregular-shaped blister generation	7 4
Figure 4.14	SEM images of medium terrace-shaped and large irregular-shaped blisters with (a) $3.02 \times 10^{24} \text{ m}^{-2}$ of fluence condition (100 eV, 30 min) and (b) $6.27 \times 10^{24} \text{ m}^{-2}$ of fluence condition (100 eV, 60 min).....	7 7
Figure 4.15	Size and number density variations of medium terrace-shaped and large irregular-shaped blisters according to incident ion fluence	7 8
Figure 4.16	SEM images of medium terrace-shaped and large irregular-shaped blisters with (a) 50 eV incident energy condition ($3.02 \times 10^{24} \text{ m}^{-2}$, 30 min),	

	(b) 100 eV incident energy condition ($3.02 \times 10^{24} \text{ m}^{-2}$, 30 min) and	
	(c) 200 eV incident energy condition ($3.02 \times 10^{24} \text{ m}^{-2}$, 30 min)	7 9
Figure 4.17	Size and number density variations of medium terrace-shaped and large irregular-shaped blisters according to incident ion energy	8 0
Figure 4.18	Incident angle of deuterium ion to side wall of small dome-shaped blister	8 3
Figure 4.19	Local angle effect for sputtering on the blister surface	8 3
Figure 4.20	Sequential diagram of blister destruction with sputtering aided bursting.	8 4
Figure 4.21	Surface SEM image of blister destruction procedure with sputtering aided bursting.....	8 4
Figure 4.22	Surface SEM images of partially destroyed medium terrace-shaped blister with irradiation conditions of (a) 100 eV, $6.27 \times 10^{24} \text{ m}^{-2}$ (60 min) and (b) 200 eV, $3.02 \times 10^{24} \text{ m}^{-2}$ (30 min)	8 6
Figure 5.1	Surface SEM images of remained large dent after ejection of sub-grain	9 0
Figure 5.2	Cross-sectional SEM image of remained large dent after sub-grain ejection	9 1
Figure 5.3	Sequential diagram for sub-grain ejection by deuterium ion irradiation on thermally pre-damaged KW-v target	9 2
Figure 5.4	(a) Surface and (b) cross sectional SEM images of deuterium ion- irradiated PW-h targets which are pre-damaged by heat flux irradiation with $T = 1698 \text{ }^\circ\text{C}$, 4.5 MW/m^2 , 200 s.....	9 5
Figure 5.5	Sequential diagram for hole structure generation by deuterium ion	

	irradiation on thermally pre-damaged PW-h target.....	9 6
Figure 5.6	Correlation between the diameter and depth of hole structure generated by deuterium ion irradiation on thermally pre-damaged PW-h target	9 7
Figure 5.7	(a) Surface and (b) cross sectional SEM images of deuterium ion-irradiated PW-h targets which are pre-damaged by heat flux irradiation with T = 1705 °C, 4.2 MW/m ² , 800 s.....	9 7
Figure 5.8	SEM images for aggravation of small dome-shaped blister by heat flux irradiation (a) deuterium ion-irradiated surface with conditions of 50 eV, 3.14 × 10 ²⁴ m ⁻² (30 min) (b) additional heat flux irradiation with conditions of T = 1703 °C, 400 s, 5 MW/m ² (1861 MJ/m ²).....	1 0 0
Figure 5.9	SEM images for aggravation of medium dome-shaped blister by heat flux irradiation (a) deuterium ion-irradiated surface with conditions of 100 eV, 3.14 × 10 ²⁴ m ⁻² (30 min) (b) additional heat flux irradiation with conditions of T = 1704 °C, 400 s, 5 MW/m ² (1976 MJ/m ²).....	1 0 1
Figure 5.10	SEM images for aggravation of large irregular-shaped blister by heat flux irradiation (a) deuterium ion-irradiated surface with conditions of 100 eV, 6.28 × 10 ²⁴ m ⁻² (60 min) (b) additional heat flux irradiation with conditions of T = 1703 °C, 400 s, 5 MW/m ² (1861 MJ/m ²).....	1 0 3

Chapter 1

Introduction

1.1 Tungsten facing with fusion plasma

Tokamaks confine hot plasma using magnetic fields to create a fusion reaction from the collision of two accelerated nuclei, such as deuterium (D) – tritium (T), D – D, and D – He³ [1]. The hot plasma has to be separated from the wall of vessel which maintain the high vacuum environments. However, because the magnetic field confinement is not perfect, certain loss of hot plasma is necessary and appeared in the form of particle and energy fluxes. Therefore, special components are needed for the protection of structure parts of tokamaks. The materials which directly contact with plasmas are called as the plasma facing materials (PFMs). To avoid an overheating of materials, the PFMs are actively cooled by the heat sink made by the copper based materials. These protecting parts which consist of PFMs and active cooling channel are called as a plasma facing components (PFCs) [2, 3]. A special part of the tokamak wall, i.e., the first wall and divertor, must overcome the highest heat and greatest particle fluxes. For the safe operation of fusion devices, PFMs must meet the following requirements:

High melting and sublimation temperature

A material with a high melting point and sublimation temperature is advantageous, as it can resist melting due to local overheating and early evaporation at high temperatures, which is caused by low vapor pressure [4–6].

High thermal conductivity

In order to withstand incoming high heat flux from hot plasma, high thermal conductivity is necessary. This conductivity should also minimally decrease with temperature.

Plasma compatibility

Contact between the PFMs and the plasma contaminates the plasma and causes poor fusion device performance. In particular, atoms that are ejected from PFMs with high atomic numbers (Z), and that are not completely ionized, change the kinetic energy of the fuel nuclei into radiation through the excitation and de-excitation of the contained electrons. This is a significant plasma cooling mechanism that can even cause complete termination of the fusion plasma. Therefore, the addition of high- Z wall materials is not permitted, and the maximum permitted concentration limits regarding high- Z materials in fusion plasma devices must be adhered to. The use of high- Z materials such as tungsten requires considerable care and plasma control, so as to ensure low PFM atom concentration in the core. High- Z wall materials also limit the operational space compared to low- Z materials [6–8].

Sputtering resistance

To reduce the erosion of the PFMs, high resistance against physical and chemical sputtering is necessary [9]. Chemical sputtering can lead to the formation of undesirable phases and influences the tritium inventory in the machine.

Tritium inventory

As a result of the limited radioactive inventory in the device, the retention of tritium is also a critical criterion. A larger amount of tritium retained in the wall materials means that less tritium is available for the fusion reaction [10, 11].

Considering the above-mentioned requirements, tungsten is currently the most promising candidate material for use as a PFM in fusion reactors such as the International Thermonuclear Experimental Reactor (ITER) and the Demonstration Power Plant (DEMO). This is because tungsten has low erosion and sputtering rates, low tritium retention, high thermal conductivity, and the highest melting point (3,422 °C) of all metals [12]. However, tungsten also has serious disadvantages such as a high atomic number ($Z = 74$), poor workability at low temperatures due to its high ductile to brittle transition temperature (DBTT), recrystallization behavior, and neutron embrittlement/activation. The characteristics of tungsten and an overview of its advantages and disadvantages are summarized in Tables 1.1 and 1.2 respectively [8, 13, 14].

Table 1.1 Characteristics of tungsten

Atomic number Z	74
Melting point	3422 °C

Max. allowable concentration in the plasma	1 ppm
Thermal conductivity at RT	173 W/m-K
Thermal expansion coefficient at RT	$4.6 \times 10^{-6}/K$

Table 1.2 Advantages and disadvantages of tungsten

Advantage	Disadvantage
high melting point	high Z
high thermal conductivity	high DBTT
low erosion rate	poor workability
low tritium retention	recrystallization
good thermal shock resistance	neutron embrittlement / activation

1.2 Energy transfer to wall material in fusion devices

A fusion plasma transfers excessive energy from the core plasma to the surrounding PFMs through the edge plasma of the fusion device. The edge plasma has good thermal and particle flux insulation characteristics. Nevertheless, the PFMs are exposed to extreme energy flux, especially in the case of the divertor. From a PFM perspective, the excessive transferred energy manifests in the form of thermal and particle effects on the plasma-facing surface of the wall material. The dominant effect on the PFM surface varies depending on the operating mode, the local characteristics of the edge plasma, and the position of the PFMs in the vacuum vessel. Specifically,

the PFM surfaces of the first wall and divertor are predominantly affected by particle and thermal effects, respectively. The following description focuses on the reliable thermal- and particle-dominant conditions with their transferred values.

1.2.1 Energy transfer by heat flux

The surface temperature increases throughout the discharge time until the energy deposition and dissipation by active cooling reach equilibrium. During a normal ITER plasma pulse, the expected heat fluxes are $\sim 0.5 \text{ MWm}^{-2}$ for the first wall and up to 20 MWm^{-2} for the divertor. Moreover, high particle fluxes degrade the mechanical and thermal properties of the materials and make it even more difficult to choose the right material for this application [15, 16]. Besides these steady-state conditions, uncontrolled electromagnetic forces and fluctuations that lead to plasma confinement instability also exist. As a result, intensive transient heat loads exist that can be classified into three main types – edge localized modes (ELMs), plasma disruptions and vertical displacement events (VDEs). An overview of selected events and their different power densities and durations is given in Figure 1.1 [17].

Edge localized modes (ELMs) are so-called normal transient events. They are common for H-mode (high-confinement mode) plasmas and lead to a periodic energy loss at the plasma edge. This occurs because the pressure gradient at the plasma edge exceeds a critical threshold and turbulent vortices can be observed. The pressure then collapses and the edge plasma is lost to the scrape-off layer (SOL), following the magnetic field lines to the divertor and depositing its energy there [18]. Type-1 or “giant” ELMs, are considered to be the most problematic in terms of PFM damage. In ITER, they are expected to deposit an energy of ca. 1 MJm^{-2} or more, with a duration

of 0.2 – 0.5 ms and a frequency of several Hz [19, 20].

Plasma disruptions are off-normal transient events. A disruption is a sudden breakdown of the plasma because of plasma confinement instability due to electromagnetic forces. After a fast thermal quench, the plasma current breaks down rapidly. This process can be divided into three phases: the precursor phase, thermal quench, and current quench. During the precursor phase, distortion of the plasma and magnetic field are induced. This leads to a rapid loss of thermal energy called a thermal quench. Finally, the plasma current decays rapidly during the current quench phase. These disruptions deposit a large amount of energy of over 30 MJm^{-2} on the PFMs within a period of $0.1 - 3 \text{ ms}$ [20].

Vertical displacement events (VDEs) are also off-normal transient events. These events are caused by the loss of vertical control of the plasma confinement, leading to a vertical drift of the plasma and plasma contact with the wall. During this contact, the plasma deposits energy of ca. 60 MJm^{-2} on the wall. Such events have a duration of between $100 - 300 \text{ ms}$ and can cause serious damage to the PFMs and components [21, 22].

1.2.2 Particle flux irradiation

Materials that will be used in fusion devices must withstand high particle fluxes that can be divided into ion, electron, and neutral fluxes. Both have similar values of over $10^{24} \text{ m}^{-2}\text{s}^{-1}$ at the plasma strike points in the divertor region. The ions follow the open magnetic field lines of the separatrix and the SOL. Taking an ITER discharge of 450 s into account, this flux leads to a total fluence of over 10^{26} m^{-2} per discharge. The plasma density is approximately 10^{21} m^{-3} and the plasma temperature is in the region of 3 eV, which corresponds to an ion impact energy of 15 eV. This is due to the acceleration between the plasma facing component (PFC) and the plasma; the so-called plasma sheath potential. These loading conditions lead to significant heating of the PFM surface from 200 – 1,500 °C in the divertor region and from 200 – 300 °C at the first wall. Note that it is much more complicated for ions to reach the first wall and the estimated flux values are quite uncertain. No open magnetic field lines exist to lead the ions to the first wall, but a small ion flux to that component does exist, which is due to neoclassical and anomalous transport. Modeling results predict a neutral flux in the range of $10^{19} - 10^{21} \text{ m}^{-2}\text{s}^{-1}$, with energies between 8 – 300 eV. Indeed, the ion flux is 3 orders of magnitude less than that of divertor region, even if long range transport through the SOL is taken into account [10].

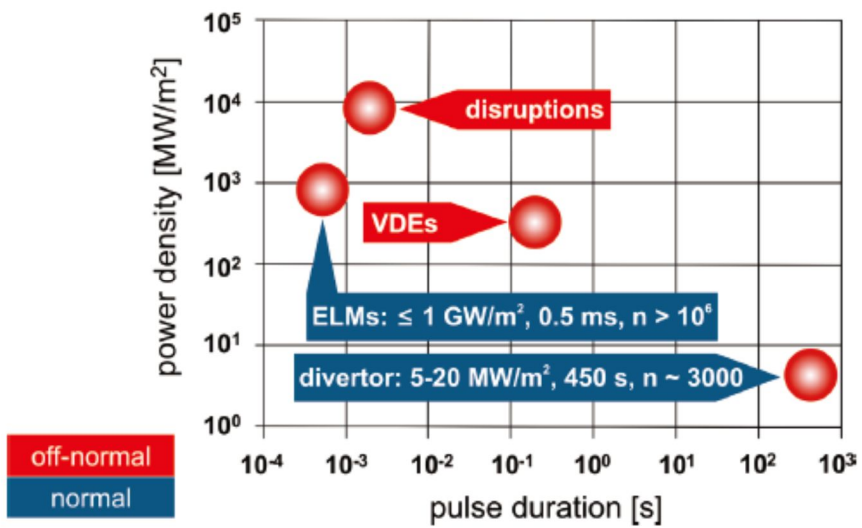


Figure 1.1 Overview of the power densities and durations of different events in ITER.

1.3 Local damages of tungsten in fusion plasma

The interaction of the hot fusion plasma and tungsten PFMs causes several types of damage on the tungsten surface due to high-energy incident particles, transferred thermal energy, and chemical reactions. The thermal effects alter the thermo-physical characteristics of the tungsten through recrystallization, melting, and sublimation. In particular, the cyclic thermal load causes mechanical stress that leads to relatively large damage features such as cracking. The particle effects alter the tungsten morphology by penetrating the tungsten. On the other hand, chemical reaction does not have a significant effect on tungsten PFMs in hydrogen and helium plasma environments.

Typical effects of thermal damage include roughening, cracking, recrystallization, and melting/sublimation, depending on the characteristics of the tungsten PFM, its surface temperature, and the intensity of the thermal loads. In a case involving thermal energy focused on a small area for a very short duration, the resultant thermal-driven damage is most prominent in the form of local melting and plasma ejection on the surfaces of the tungsten PFMs [23–25]. The transfer of thermal energy causes mechanical stress through the repetition of high thermal loads, as can be seen during ELMy H-mode operation of the tokamak. The thermally induced mechanical stress causes local cracks on the tungsten PFMs with a thickness ranging from a few micrometers to the order of millimeters [26–34]. High-temperature environments, which are created by the steady state or transient thermal energy transfer, cause variations in the grain structure of tungsten PFMs. The change of grains, so called recrystallization, is occurred with enlarged and newly distributed grains. The recrystallization is proceeded at a temperature condition of over 1300 °C

accompanying with a recovery of deformation and growth of small sub-grains [35, 36]. At the higher temperature condition, the recrystallization requires the shorter transition time. On the recrystallized surface of tungsten, a different crystallographic orientation is formed or rearranged by the boundaries which separate a specific region. According to a misorientation between the two grains, the recrystallized grains are divided to a grain and a sub-grain. Generally the high angle boundary has greater misorientation angle than 15° . On the other hands, the low angle boundary shows less angle than 15° . As a very general guide, low angle boundaries is considered to be composed of dislocation array and whose structure and properties vary as a function of misorientation. Whereas, structure and properties of high angle boundaries are not generally dependent on the misorientation [36]. In the view of mechanical properties, Recrystallized tungsten exhibits significant property changes such as reduced hardness and increased embrittlement [37]. These property changes are important as regards the understanding of plasma and material interaction from the thermal energy perspective.

Contrary to the thermal energy transfer, incident particles remarkably alter the surface of tungsten PFMs with not affected material properties of bulk tungsten. Light ions such as hydrogen isotopes and helium are mainly incident on the tungsten surface from the fusion plasma with relatively low bombardment energy of a few hundred electron volts. The incident ions are stopped at a thickness range of a few tens of nanometers and diffuse toward the deeper regions within the tungsten. In this region, the crystallographic defects of tungsten such as an interstitial, vacancy, dislocation and grain boundary trap the diffused hydrogen isotope. The trapping of hydrogen isotope aggravates the defects, leading to a nano void, nano / micro cracks, deformations and slipping [38]. Eventually, a blister like structure is generated from these aggravated

defects [39–44]. The blister like structures show are strongly depends on the incident conditions of ion such as ion species, impact energy, flux of ion, fluence of ion and surface temperature [40, 45–48]. In addition, the material properties of tungsten, such as grain size, texture and defects (dislocations, vacancies and voids), are also an important factor for the morphology of blister like structures [39]. Especially, the properties of defects is most important factor for a determination of blister shapes near the surface of tungsten.

1.4 Objectives

The purpose of this dissertation is to understand tungsten surface-damage generation under the conditions of a nuclear-fusion-plasma-relevant environment. The damage generation mechanism is studied by considering plasma characteristics such as thermal-effect- and particle-interaction-dominant conditions. In addition, the material characteristics are considered in order to analyze the damage characteristics I response to variations in the tungsten target grain structures.

Surface damage on tungsten PFMs is caused by thermal effects due to the high heat-flux irradiation facility in tokamaks. This facility provides the heat-flux conditions required by the ITER divertor for steady state operation. Recrystallization occurs prominently on the heat-flux irradiated surfaces of tungsten targets and is characterized by the transferred thermal energy. The heat-flux irradiation creates a temperature gradient from the surface to the bottom of the target. As regards this temperature distribution within the target, the resultant internal damage to the target is discussed by considering the direction of the near-surface grain, i.e., vertical or horizontal elongation.

Deuterium ions are irradiated on the surface of a tungsten target using the ion flux irradiation facility, and the deuterium-ion-irradiated surface is then morphologically changed to a blister-rich surface. The blisters are characterized based on the fluence and incident energy of the deuterium ions, which make contact with two target types (with either vertically or horizontally elongated grains). The destruction of these blisters is discussed in relation to sputtering increment and morphological variation.

The surface damage induced by heat and ion flux irradiation is aggravated by additional ion and heat-flux irradiation. The evolution of the damage sustained by a high-heat-flux-irradiated target is examined using deuterium-ion irradiation and considering both grain direction and internal target damage features such as cracks and bubbles. The destruction of blisters generated by deuterium-ion irradiation is discussed using the heat-flux irradiation of two target types, i.e., targets with vertically or horizontally elongated grains.

Chapter 2

Experimental Setup

2.1 Heat flux irradiation facility

2.1.1 High power thermal plasma torch

As a heating source for the irradiation of high heat flux to the tungsten target, a high-power plasma torch is equipped with non-transferred-type hollow electrodes. Figure 2.1 shows a cross section of the plasma torch with hollow electrodes used in this work. The two cylindrical electrodes are composed of oxygen-free high purity (OFHP) copper for sufficiently high electric and heat conductivity. The rear well-type cylinder with a closing end wall functions as a cathode (-) and the front hollow cylinder with open ends serves as an anode (+). The length of each electrode has a significant effect on the electrode lifetimes and the thermal efficiency of the torch. A short electrode length leads to a severe erosion problem near the end wall of the cathode and heavy damage to the external body of the torch, due to the narrow axial area compared with the arc length. In contrast, a long electrode length causes heat loss that is increased by the coolant water flowing around the electrodes, due to the large interior electrode area. Generally, the arc length and corresponding voltage in a hollow-electrode plasma torch are larger than those in a rod-nozzle-type plasma torch.

Therefore, the hollow-electrode plasma torch has lower thermal

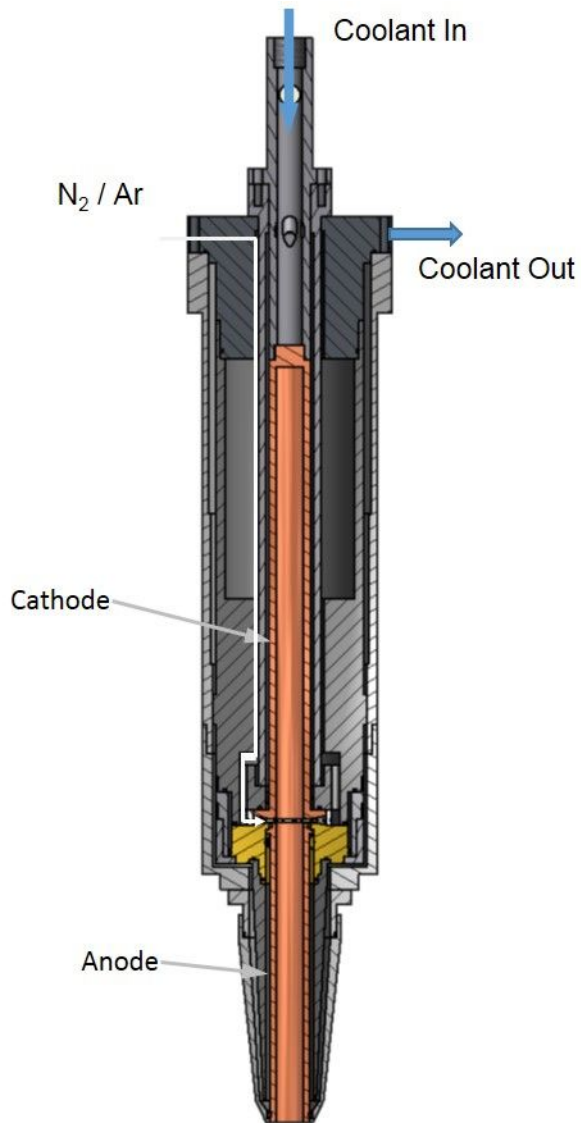


Figure 2.1 Design of hollow electrode thermal plasma torch

efficiency than the rod-nozzle-type torch, due to the greater heat loss caused by the long electrode length. However, since the hollow-electrode torch input power can be enhanced easily, it produces a large volume of thermal plasma flame compared to the rod-nozzle-type electrode torch [49]. Therefore, the thermal plasma torch with hollow electrodes, which has the advantage of generating higher-power thermal plasma, is used in the present work.

In order to confine the arc roots within the cylindrical wall surface of each electrode, the appropriate electrode lengths are experimentally determined to be 300 and 200 mm for the cathode and anode, respectively. To obtain stable arc attachment, the electrode diameter is controlled while ensuring sufficiently high temperature and electric conductivity inside the discharge area. Further, to prevent abrupt disruption of the arc discharge caused by insufficient gas temperature inside the discharge region, the electrode diameter is limited to within a specific range. From the results of the hollow-electrode torch performance experiments, electrodes with diameters of less than 18 mm exhibit stable arc discharge under various operation conditions. Therefore, a fixed diameter of 18 mm is used for the electrodes in the present work. To prevent thermal damage to the torch components from the high heat flux from the arc discharge, the coolant water, which is supplied by a pressurized water circulation system, actively cools the cathode and anode while, for easy electrical breakdown between the two electrodes, the electrodes are set to maintain a narrow gap of 2 mm using a gas injection ring. The gas injection ring, which is composed of ceramic material (Alumina, Al_2O_3) has 12 annular holes around its circumference that allow it to inject plasma-forming gas evenly. These holes are bored at an angle of 35° inclined to the radial direction in order to produce a vortex motion in the plasma-forming gas.

This is a well-known technique for stabilizing arc discharge.

2.1.2 Target holder

The tungsten target holder was designed as illustrated in Figure 2.2 and Figure 2.3, which are a schematic diagram of the holder and a manufacturing design drawing, respectively. The holder is optimized to a fixed 10-mm diameter and has adjustable thickness from 1 – 10 mm. The target is mechanically fixed by a cap that is cooled by the pressurized coolant water with a mass flow rate of 25 lpm. The cap applies pressure to the target from the surface and makes contact between the target and beneath holder. The contact area is determined by considering stable fixing and the exposed surface area to the thermal plasma jet. The diameter of the exposed area is 8 mm, which is the standard size for the calculation of heat flux and thermal conduction analysis. The backside of the tungsten target is cooled by an active cooling system that supplies pressurized coolant water with a flow rate of 0.1 – 1 lpm and maintains the water temperature at a constant value. The target is separated from the active cooling channel by a stainless steel supporting structure. The gap between the backside of the target and the stainless steel support is filled with two functional parts: a thermocouple-aided heat-flux sensor and a ceramic disk spacer, which control the total thermal conductivity of the target backside (its cooling capacity) and prevent thermal adhesion between the target backside and heat-flux sensor, respectively. Three kinds of ceramics: zirconia, alumina, and silicon carbide are used in the ceramic spacer.

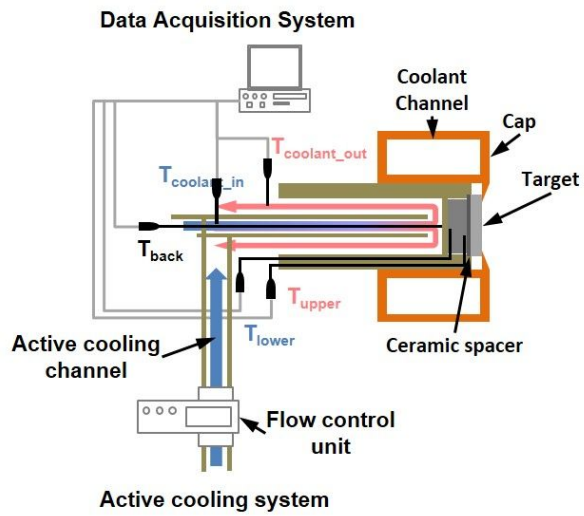


Figure 2.2 Schematic diagram of substrate holder

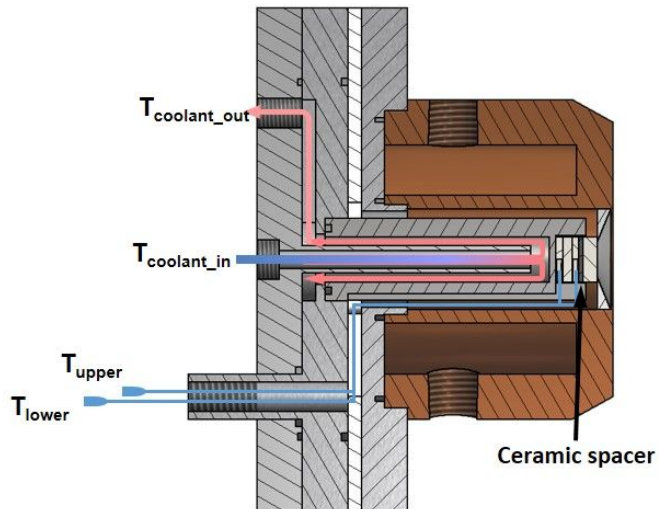


Figure 2.3 Design of substrate holder

2.1.3 Temperature measurement

A pyrometer is used to measure the surface temperatures of the tungsten targets during heat-flux irradiation. A Metis MI16 pyrometer from Sensortherm GmbH monitors the surface temperature of the target tungsten. It operates with a single wavelength of 1.6 μm and over a range of 500 – 2,500 $^{\circ}\text{C}$. Thermal radiation emitted from the surface is transformed into an electric signal, S , through the amplifier, analog to digital convertor (ADC), compensating processor, and digital to analog convertor (DAC), as depicted in Figure 2.4. This electrical signal is represented as a voltage, governed by Plank's law, and is expressed as

$$S = C\varepsilon \frac{2hc^2}{\lambda^5} \frac{1}{e^{\left(\frac{hc}{k_B\lambda T}\right)} - 1} \quad [\text{V}] \quad (2.1)$$

where C is the system factor containing the amplification ratio (between the conversion efficiencies of ADC and DAC), h , c , λ , and k_B are the Planck constant, the speed of light, the measuring wavelength, and the Boltzmann constant, respectively. The ε term represents the emissivity of the target tungsten surface. The converted digital signal is modified by this surface emissivity, which varies according to the surface conditions, e.g., roughness, temperature, and measuring wavelength. In this study, $\varepsilon = 0.24$ is used for a polished tungsten surface.

Thermo-couples are used for the other temperature measurement components such as coolant-temperature and heat-flux sensors. All the thermo-couples are type K from OMEGATM with a range of 200 – 1,350 $^{\circ}\text{C}$.

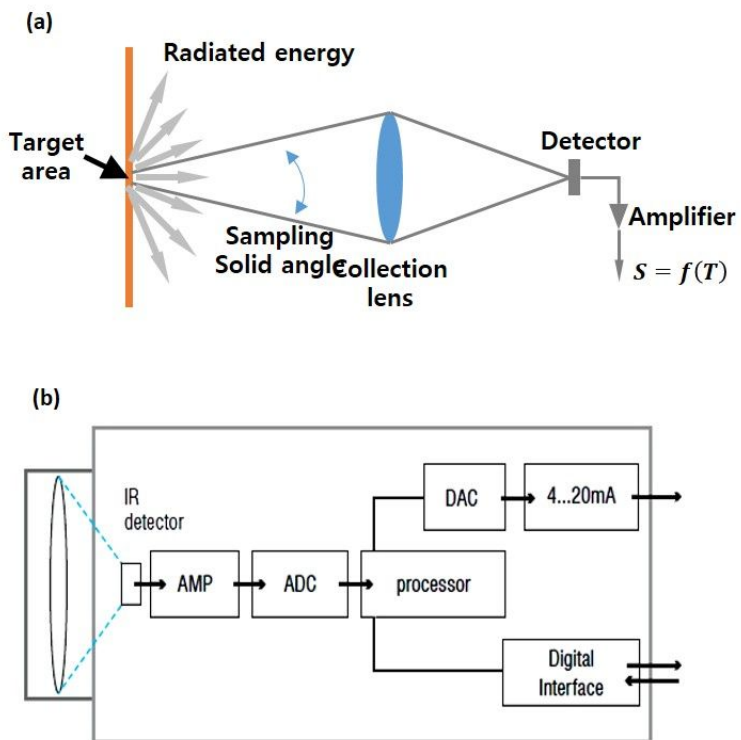


Figure 2.4 (a) Schematic diagram of surface temperature measurement and
 (b) flow chart of temperature calculation in pyrometer

2.1.4 Heat flux measurement

The heat flux irradiated onto the target surface is measured using the two methods, shown in Figure 2.5: the calorimetry method using the active cooling channel and the thermo-couple-aided heat-flux sensor. In the calorimetry method, the heat flux is calculated using the coolant water flow rate and the temperature difference between the coolant inlet and outlet. The flow rate is controlled by the flow control unit, which has a range of 0.1 – 1.5 lpm. The inlet and outlet coolant temperatures are measured by K-type thermo-couples. The measured data are used to calculate the heat flux, q , according to

$$q = \frac{Q}{A} = \frac{1}{A} \frac{m}{\Delta t} C_{water} (T_{outlet} - T_{inlet}) \quad (2.2)$$

here, A and C_{water} are the exposed target area and the specific heat of the water, respectively, while $\frac{m}{\Delta t}$ is the coolant flow rate, and T_{outlet} and T_{inlet} are the outlet and inlet coolant temperatures, respectively.

Another heat-flux measurement sensor is placed at the backside of the ceramic disk spacer and is composed of two thermo-couple-implanted tungsten disks and a tungsten spacer to create a temperature difference. The tungsten disks are placed on either surface of the tungsten spacer, which has a thickness of 2 mm, as depicted in Figure 2.4. The K-type thermo-couples are located at the center of the disk, in terms of both diameter and thickness. The measured temperature data is then converted to the heat flux using

$$q = \frac{Q}{A} = \frac{1}{A} k \frac{(T_{upper} - T_{lower})}{\Delta x} \quad (2.3)$$

where k and Δx are the thermal conductivity and the distance between the two temperature measurement points, respectively, A is as previously defined, and T_{upper}

and T_{lower} are the upper and lower temperatures as measured by the thermo-couple-implanted disks, respectively. The measured heat fluxes are compared with each other in order to confirm the measurement accuracy.

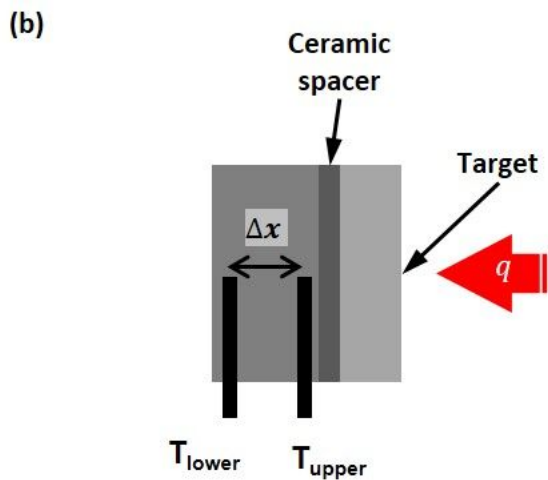
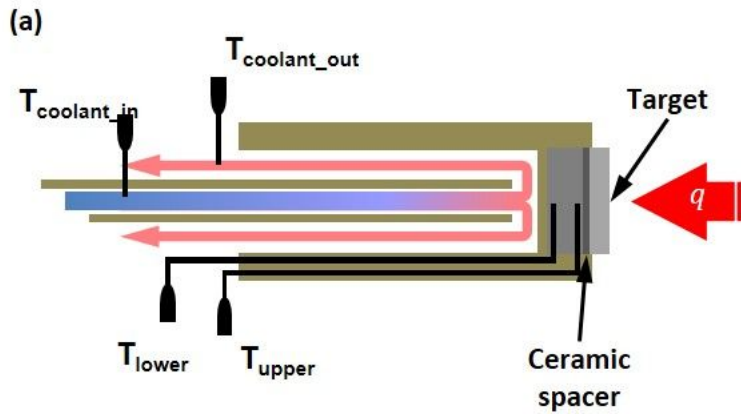


**Figure 2.5 Schematic diagram of heat flux measurements by
(a) calorimetry of coolant and (b) heat transfer in disk**

2.1.5 Operating Characteristics

A schematic diagram and photograph of the heat-flux irradiation facility are given in Figure 2.6 and Figure 2.7, respectively. The hollow-electrode thermal plasma torch and the target holder are installed facing each other in the vacuum chamber. The distance from the torch exit to the target surface is varied in order to control the heat flux and temperature. The operation of heat-flux irradiation facility is performed at a base pressure of 3×10^{-2} Torr and an operating pressure range of 50 – 200 Torr, to prevent oxidation of the target surface. Since the thermal plasma torch requires a specific ignition sequence, the heat-flux irradiation facility is operated in four different phases: ignition, lamp power-up, heat-flux irradiation, and target cooling, as shown in Figure 2.8. During the ignition phase, the thermal plasma torch is ignited with 140 slpm of Ar and a 100 A discharge current under a pressure of 100 Torr. For stable ignition, pure Ar is used as a discharge gas in the ignition phase. The generated pure Ar thermal plasma is changed to pure N₂ plasma in the next phase: the lamp power-up stage. The Ar supply is gradually reduced to zero and replaced by N₂ gas, the flow rate of which is gradually increased to yield full concentration. The discharge current is simultaneously increased in accordance with the increasing N₂ content. For minimum erosion of the electrode, full N₂ discharge is achieved before the discharge current reaches 150 A. The N₂ flow rate and current are increased to a specific condition to obtain the required surface temperature and heat flux. The plasma power is increased by an extended arc length and high current value. At the precise moment when the temperature and heat flux reach the required conditions, the heat-flux irradiation phase and the irradiation time count begin. The plasma power is maintained during this phase. At the end of the irradiation phase, the thermal plasma torch is turned off and

the tungsten target is immediately cooled to room temperature.

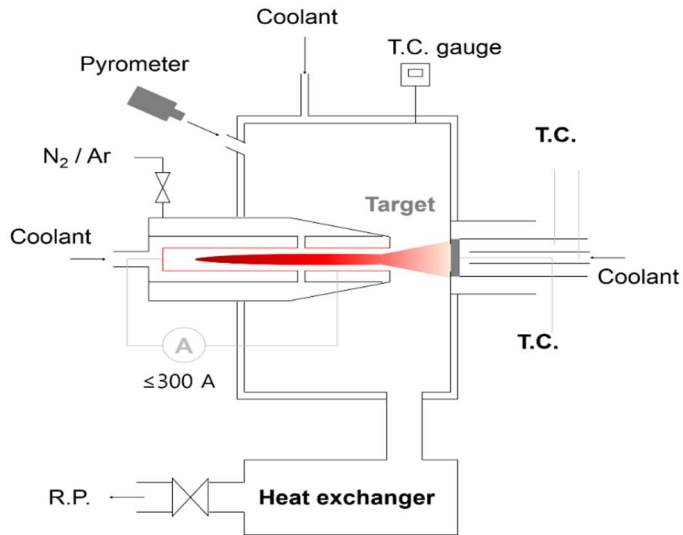


Figure 2.6 Schematic diagram of heat flux irradiation facility

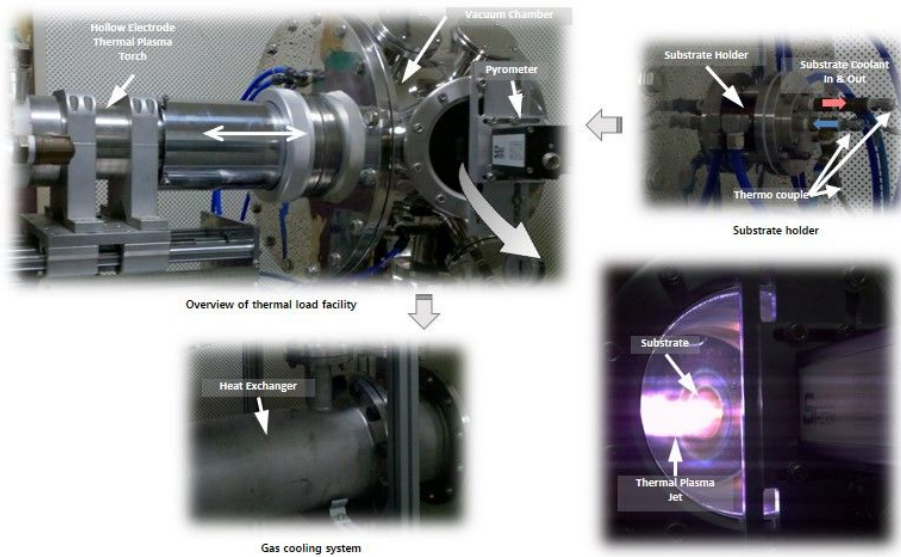


Figure 2.7 Picture of heat flux irradiation facility

This is the target cooling phase. The most stable operating condition is found to be 190 A discharge current and 230 slpm N_2 gas flow. Under these operating conditions, the distance from the torch exit to the target determines the heat flux and temperature, as shown in Figure 2.9 and Figure 2.10. As the distance decreases, the heat flux is increased exponentially. However, in the interests of safety, the distance is limited to 50 mm. At a distance of less than 50 mm, the arc plasma can make direct contact with the tungsten target and a forced shutdown will occur. In the case of a shorter distance and with a higher heat-flux increment, the target surface approaches a higher temperature. At 50 mm, the heat flux and surface temperature can be adjusted by varying the gas flow rate, discharge current, and the ceramic disk spacer (which is placed at the backside of the tungsten target). The heat flux is higher in a SiC spacer than in an Al_2O_3 spacer for the same tungsten target surface temperature, because SiC has greater thermal conductivity than Al_2O_3 . To obtain the required heat flux and temperature, the

distance and ceramic spacer type are first decided, and then the gas flow rate and discharge current are adjusted in order to control the temperature and heat flux precisely.

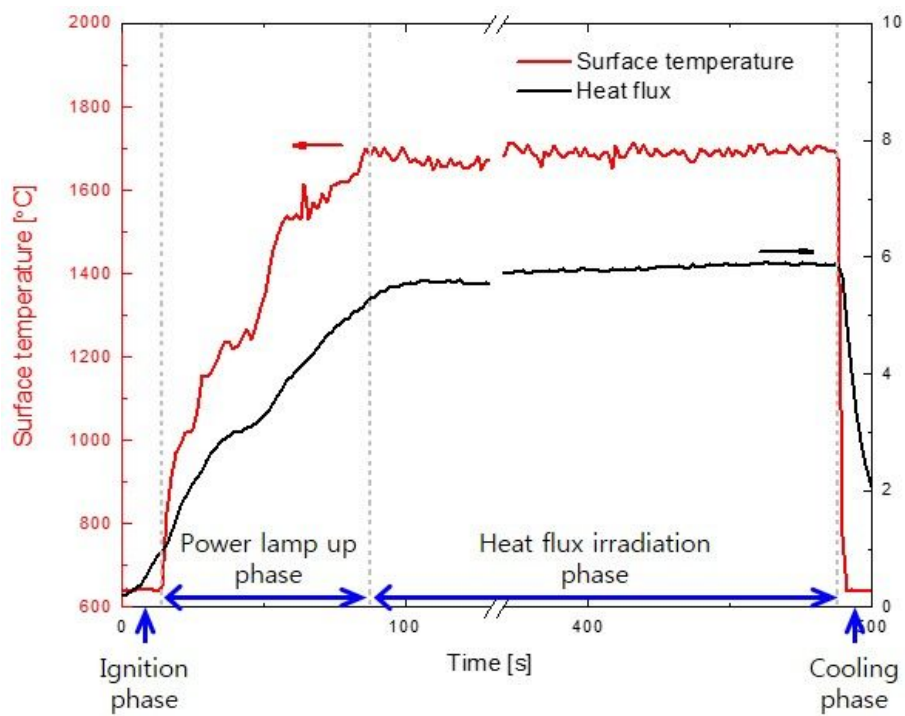


Figure 2.8 Operating sequence of heat flux irradiations using hollow electrode thermal plasma torch

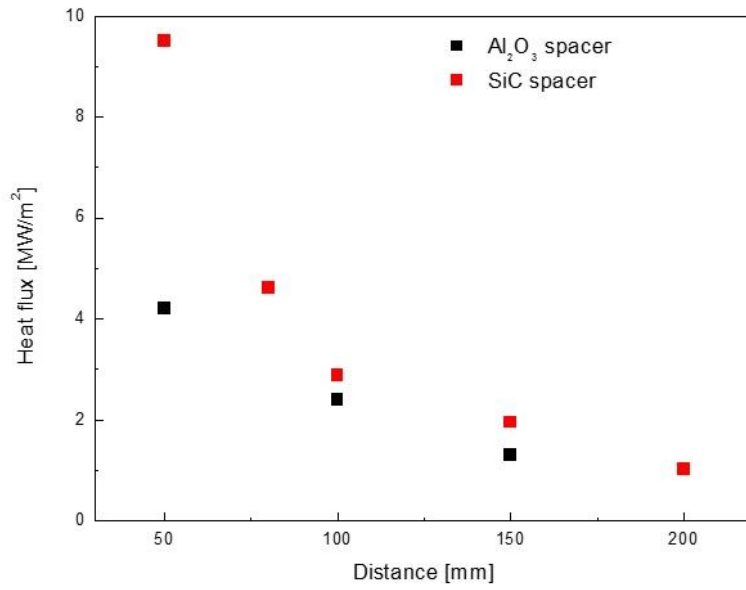


Figure 2.9 Variation of thermal loads according to substrate position

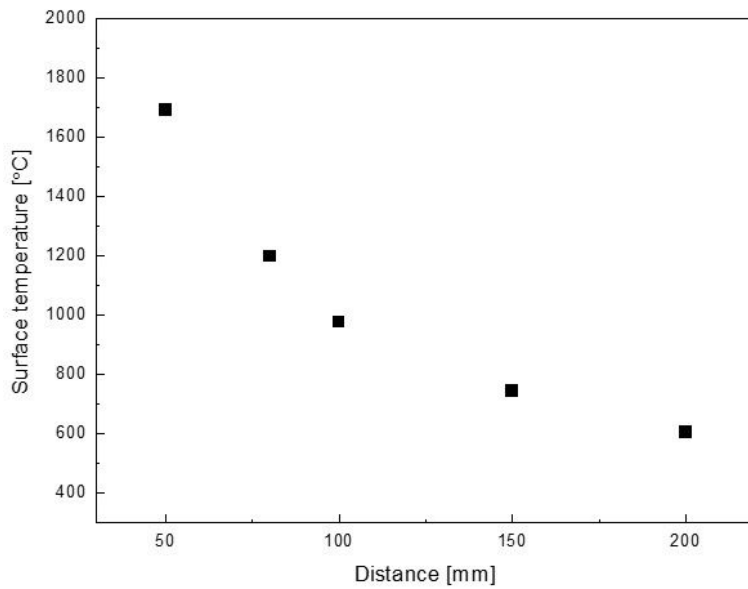


Figure 2.10 Variation of surface temperature according to substrate position

2.2 Ion flux irradiation facility

2.2.1 Electron cyclotron resonance plasma generator

An electron cyclotron resonance (ECR) plasma generator is used for the generation of deuterium ions. The generated deuterium ions are drawn to the tungsten target by the bias voltage, which is DC or pulsed. A schematic diagram of the deuterium-ion flux irradiation facility is given in Figure 2.11. The facility consists of an ECR plasma source chamber, an external coil for the generation of a magnetic field, and a downstream chamber for ion drawing. The ECR plasma source chamber is composed of stainless steel and has a diameter of 18 cm and a height of 12 cm. A quartz plate is placed on top of the aluminum chamber and acts as a microwave path. The microwaves are supplied to the plasma chamber from above by a 2.45 GHz power source (SGM-15A, DAIHEN). To direct this zero-reflection power, the microwaves are transferred efficiently through a model CMC-10 auto-matching network produced by DAIHEN. Two external coils are installed outside the ECR plasma source chamber; the top coil begins above the quartz plate at a 7 cm distance and the bottom coil is installed directly below the top coil. The downstream chamber is composed of stainless steel with a diameter and height of 400 and 300 cm, respectively. At the center of the downstream chamber, the target holder is located at a distance of 7 cm from the ECR plasma source chamber.

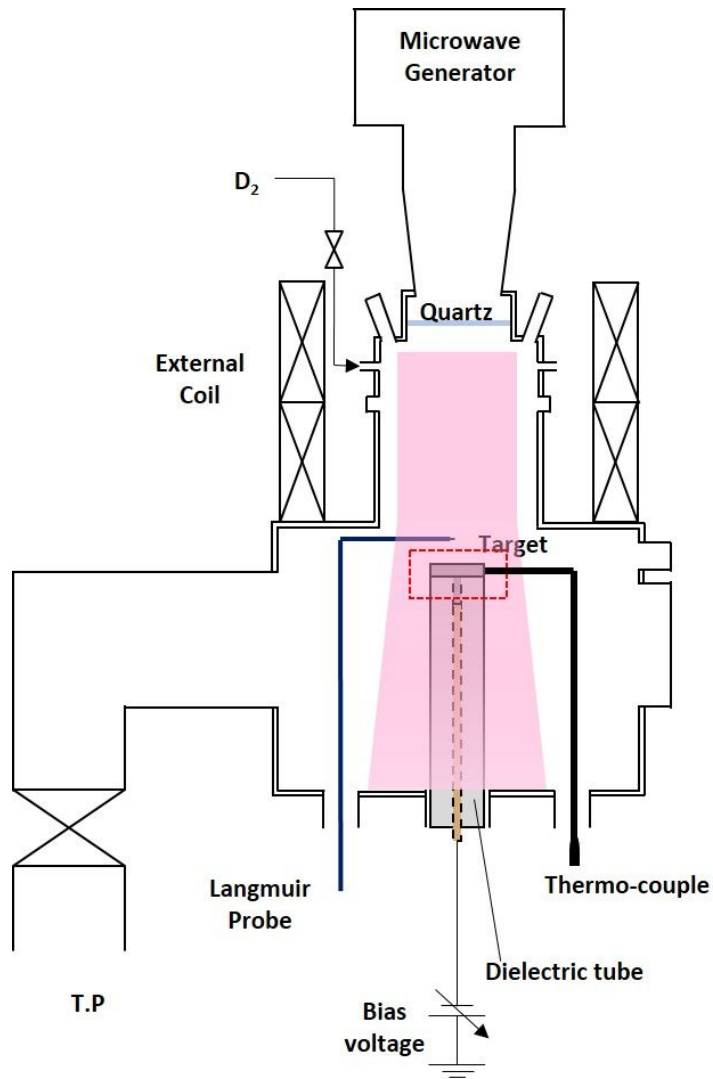


Figure 2.11 Schematic diagram of deuterium ion irradiation facility

2.2.2 Target holder

The target holder is composed of stainless steel circular plates of 35 mm in diameter and 5 mm in thickness. The tungsten target, which is coin-shaped and has a diameter of 10 mm and thickness of 3 mm, is installed in a hole in the circular plate, as shown in Figure 2.12. Four tungsten targets can be simultaneously irradiated by the deuterium-ion flux under the same irradiation conditions. The temperature of each target is monitored by a contact thermo-couple positioned at the target side. The circular plate is connected to a copper post, which is insulated by a ceramic cylinder, so that the bias voltage can be applied to the target tungsten.

2.2.3 Deuterium-ion flux characteristics

For the production of deuterium ions, the ECR deuterium plasma is generated with 400-W microwave power, 100 A external coil current, and 1 mTorr operating pressure. A DC voltage is applied to the circular target plate through the copper post with a voltage ranging from -183 – -33 V. The applied bias voltage causes the deuterium ions, which are generated in the ECR plasma source chamber, to be drawn to the circular target plate with 50 – 200 eV impact energy. The incident deuterium ions consist of three kinds of ion: D^+ , D_2^+ , and D_3^+ , and the exact concentration of each ion type is determined by the operating pressure and the plasma dissipation power [50]. Under these operating conditions (1 mTorr pressure and 400 W plasma power) the plasma contains deuterium ions with D^+ , D_2^+ , and D_3^+ concentrations of 37.1, 42.9, and 20%, respectively [51]. Therefore, the incident deuterium ions also have the same ratio as the ions in the ECR plasma source chamber. To characterize the plasma at the front of the target surface, a Langmuir probe is used to measure the plasma properties. The

measured values of the plasma properties are a plasma density of $9.2 \times 10^{16} - 1.3 \times 10^{17} \text{ m}^{-3}$ and an electron temperature of $4.8 - 5.5 \text{ eV}$. From these plasma parameters, the incident ion flux is estimated using the Bohm flux model and found to be within a range of $1.67 - 2.93 \times 10^{21} \text{ m}^{-2}\text{s}^{-1}$. These plasma characteristics have values of similar order to those of the Korea Superconducting Tokamak Advanced Research (KSTAR) SOL plasma, which has a plasma density of $1.3 \times 10^{17} \text{ m}^{-3}$, an electron temperature of 4 eV , and an ion flux of $3.46 \times 10^{21} \text{ m}^{-2}\text{s}^{-1}$ [52]. The total fluence of the deuterium-ion irradiation is controlled by the irradiation time to within a range of $1.0 \times 10^{24} - 2.38 \times 10^{25} \text{ m}^{-2}$. The abovementioned specific ion irradiation parameters are summarized in Table 2.1.

Table 2.1 Ion irradiation conditions

Plasma density	$9.2 \times 10^{16} - 1.3 \times 10^{17} \text{ m}^{-3}$
Electron temperature	$4.8 - 5.5 \text{ eV}$
Ion flux	$1.67 - 2.93 \times 10^{21} \text{ m}^{-2}\text{s}^{-1}$
Fluence	$1.0 \times 10^{24} - 2.38 \times 10^{25} \text{ m}^{-2}$

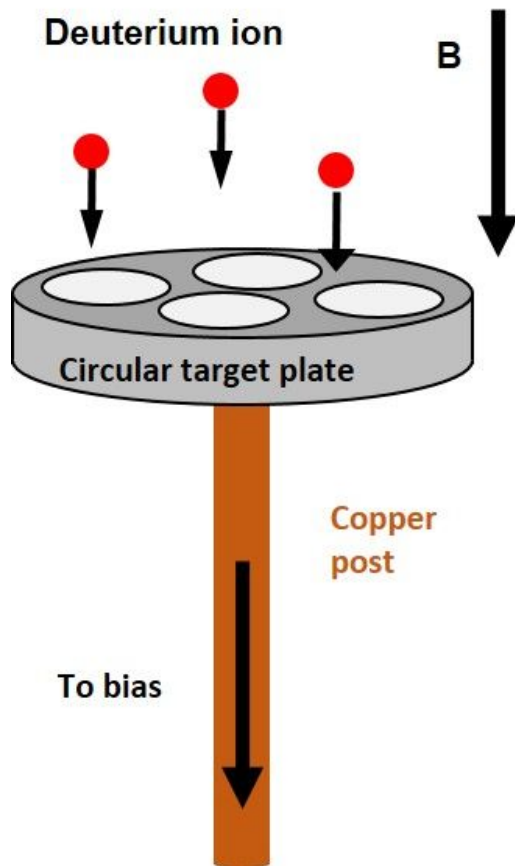


Figure 2.12 Schematic diagram of the target holder for deuterium ion irradiation

2.3 Target materials

2.3.1 Tungsten target type

The grain structure of the tungsten target is determined by the manufacturing and formation methods. Generally, the tungsten is manufactured by a powder metallurgy process, as shown in Figure 2.13 [17]. The raw material for the tungsten target is tungsten oxide (30 – 70% WO_3), which is refined to tungsten powder by oxide reduction using hydrogen. Through pressing and sintering, the tungsten powder is consolidated into a sintered block. After sintering, the final tungsten block is formed by rolling, swaging, hammering, and forging, in order to increase the density and to improve the material properties. Depending on the formation process, the grain structure has large variations. In this study, tungsten targets created using two formation methods, swaging and rolling, are used. The swaged tungsten has a vertically elongated grain structure along the target surface, while the rolled tungsten exhibits a horizontally elongated grain structure along the target surface. Korea Tungsten Co., Ltd (Korea), supplies swaged and rolled tungsten with a tungsten purity of 99.95%, while the Plansee Group (Austria) offers rolled tungsten with a higher tungsten purity of 99.98%. The tungsten targets used here are labeled KW-v, KW-h, and PW-h, indicating targets produced by Korea Tungsten Co., Ltd with a vertically elongated grain, by Korea Tungsten Co., Ltd with a horizontally elongated grain, and by the Plansee Group with a horizontally elongated grain, respectively. The grain structures of the three tungsten targets were examined using the electron backscatter diffraction (EBSD) method (EBSD system, TSL with FE-SEM, Hitachi SU-70) and the obtained grain orientation maps and grain boundary misorientation angle

distributions are depicted in Figure 2.14. The KW-v target has an average grain size of 16.7 μm , while the PW-h and KW-h targets have average grain sizes of 10.5 and 11.9 μm respectively. Both targets with horizontally elongated grains exhibit similar grain orientations and misorientation angle distributions. Thus, the PW-h target is primarily discussed in the following descriptions of the results as a representative horizontally elongated grain sample. The above-mentioned target properties are summarized in Table 2.2. Note that all the tungsten targets used in this research have diameters of 10 mm and 3-mm thickness. The holders in the deuterium-ion and heat-flux irradiation facilities are designed according to the target sizes.

Table 2.2 Characteristics of tungsten targets.

	KW-v	KW-h	PW-h
Manufacturer	Korea tungsten	Korea tungsten	Plansee Group (Austria)
Composition	W 99.95%	W 99.95%	W 99.98%
Manufacturing method	powder metallurgy	powder metallurgy	powder metallurgy
Forming Method	swaging	cold rolling	cold rolling
Post process	-	-	-
Grain structure	vertically elongated	horizontally elongated	horizontally elongated

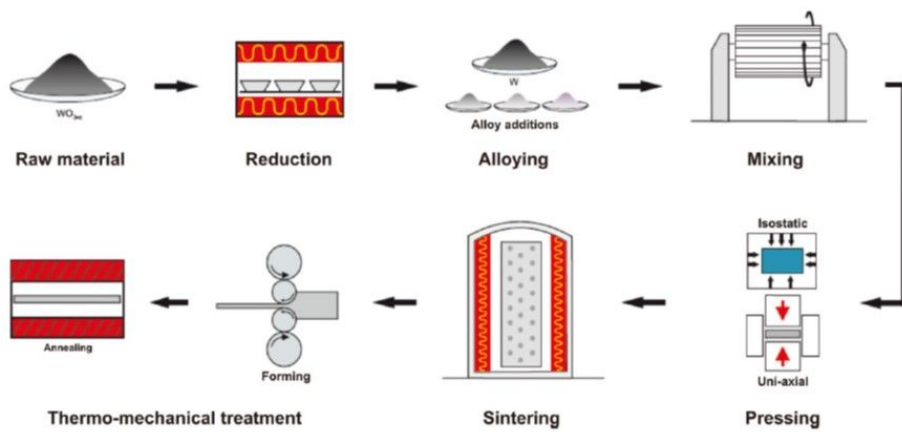


Figure 2.13 Schematic diagram of the basic powder metallurgical production process of tungsten

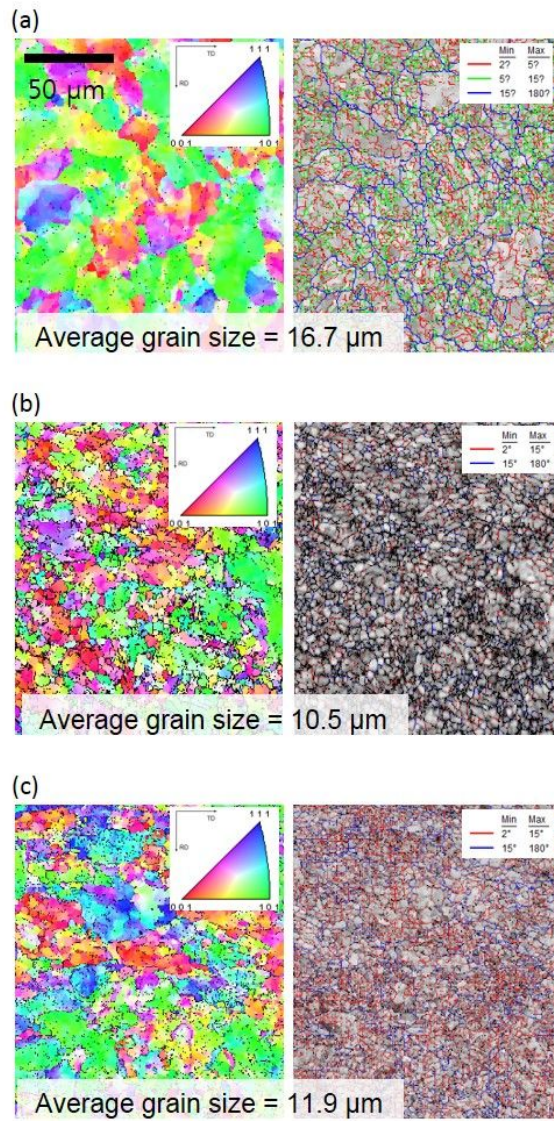


Figure 2.14 Grain orientation map and grain boundary misorientation angle distributions of

(a) vertically elongated W – KW-v, (b) horizontally elongated W – PW-h and

(c) horizontally elongated W – KW-h

2.3.2 Surface finishing method

In this study, the surfaces of all the tungsten targets were given a mirror finish in order to reduce the effects of any mechanical fabrication damage. This process was accomplished through three consecutive steps: plane grinding, fine grinding, and surface polishing. All steps were conducted using an auto polisher (Tegrmin 20, Struers) which processes four targets simultaneously. The plain grinding was conducted using SiC paper with roughness of up to P800 (using the European FEPA (Federation of European Producers of Abrasives) P-grade). The fine grinding was accomplished using a fine SiC paper with roughness of up to P2000. The last step, the polishing, was conducted using a polishing cloth and diamond suspension with particle sizes of 9, 6, 3, and 1 μm . Colloidal silica was used for the final grinding with 0.04 μm particle size. After each process, the targets were cleaned using an ultrasonic cleaner with ethyl alcohol and acetone. The specific grinding and polishing conditions are given in Table 2.3.

Table 2.3 Grinding and polishing conditions for tungsten target finishing

Step	Grinding conditions					
	SiC type	Time	Force	Rotation direction	Stage rotation	Head rotation
Plane grinding	220	30 s	15 N	Co rotation	120 rpm	120 rpm
	400	1 min	15 N			
	600	5 min	10 N			
	800	5 min	10 N			
Fine grinding	1000	7.5 min	10 N			
	1500	7.5 min	10 N			
	2000	10 min	10 N			
Step	Polishing conditions					
	Abrasive	Time	Force	Rotation direction	Stage rotation	Head rotation
Polishing	Diamond / 9 μm	20 min	30 N	Counter rotation	300 rpm	150 rpm
	Diamond / 6 μm	10 min	20 N		300 rpm	
	Diamond / 3 μm	10 min	20 N		300 rpm	
	Diamond / 1 μm	7 min	20 N		250 rpm	
	colloidal silica / 0.04 μm	5 min	5 N		150 rpm	

Chapter 3

Thermal-Driven Target surface damages

3.1 Characteristics of recrystallized target surface

3.1.1 Tungsten target recrystallization

The tungsten target was thermally irradiated at a heat flux of 4.1 MW/m^2 , which corresponds to a transferred energy of 828 MJ/m^2 . The temperature of the target surface was maintained at $\sim 1,700 \text{ }^\circ\text{C}$ over an irradiation time of 200 s. The irradiated target surface was then changed to a fully recrystallized grain structure, as shown in FE-SEM image (Figure 3.1). From the EBSD results shown in Figure 3.1 (c) and (d), the average grain size changed from $10.5 \text{ }\mu\text{m}$ (for the as-received target surface) to $29.2 \text{ }\mu\text{m}$. The as-received tungsten target contained a large number of sub-grains, which were enlarged but reduced in number. Grains with a [111] orientation disappeared from the recrystallized surface, due to the compressive stress on the top surface caused by the vertical temperature gradient. The target surface was roughened in a specific pattern depending on the grain orientation, and the grain boundary was clearer on the recrystallized target surface than on the as-received target surface, because of the thermal grooving of the grain boundary shown in Figure 3.2. In order to reduce the area and surface free energy, the grain boundary was shrunk through the

surface diffusion of tungsten atoms [53, 54].

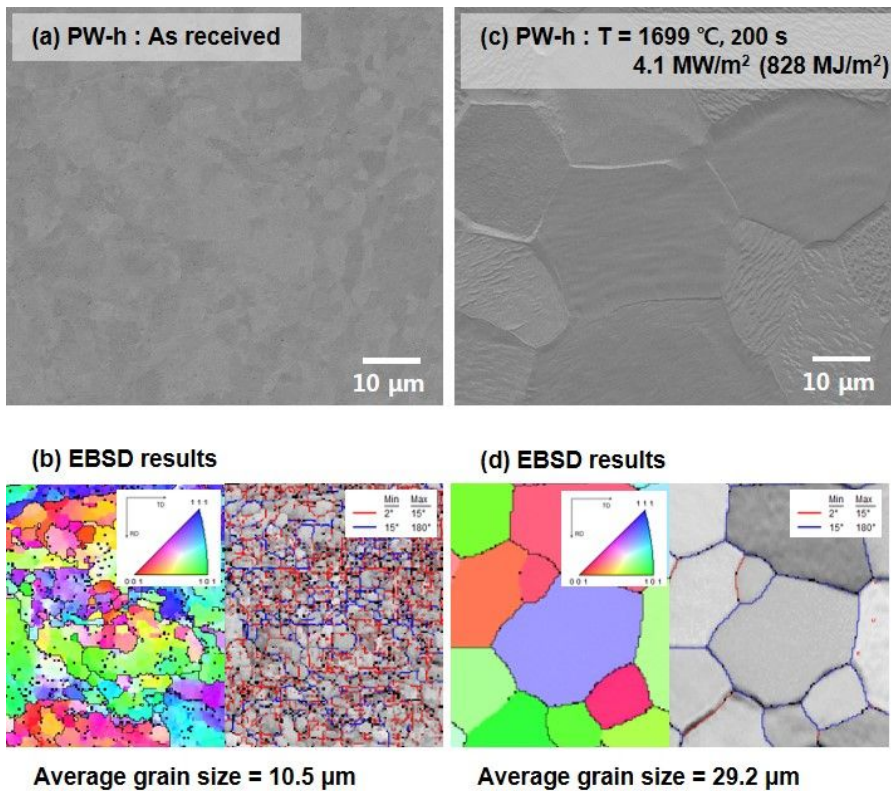


Figure 3.1 Change of Grain Structure by Heat Flux Irradiation

(a) Surface SEM image and (b) EBSD analysis results of as received PW-h target

(c) Surface SEM image and (d) EBSD analysis results of recrystallized PW-h with 1699 °C, 200 s
and 4.1 MW/m² (828 MJ/m²)

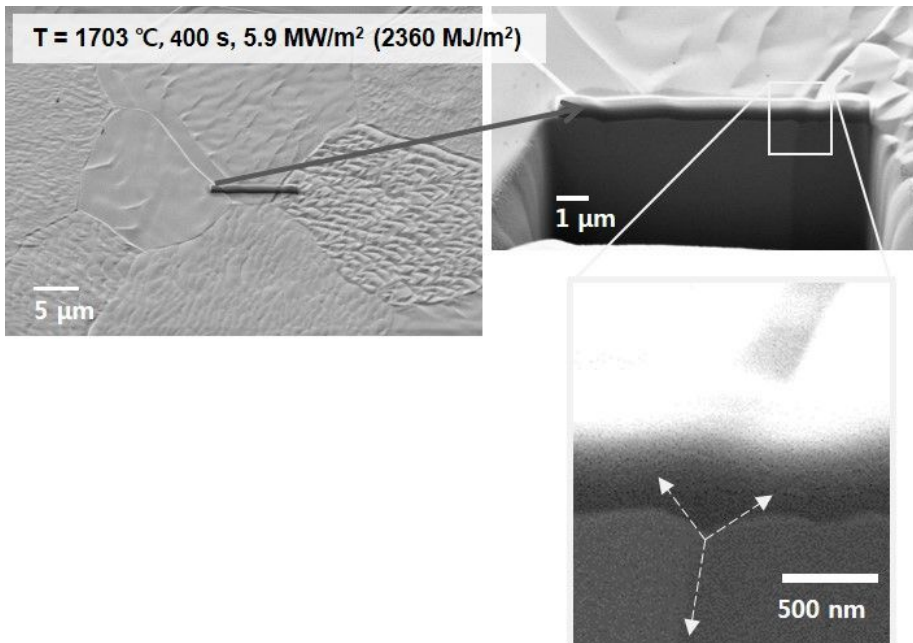


Figure 3.2 Thermal grooving of grain boundary in recrystallized PW-h target with conditions of

$T = 1703\text{ °C}$, 400 s , 5.9 MW/m^2 (2360 MJ/m²)

3.1.2 Recrystallized grain characteristics under various heat-flux irradiation conditions

To investigate the effect of irradiation time on the thermally irradiated target, the heat-flux irradiation time was varied from 50 – 420 s, which is comparable to a transferred energy of 205 – 2,500 MJ/m². During the heat-flux irradiation, the surface temperatures of all targets were maintained at approximately 1,700 °C. The effect of the heat-flux irradiation on grain size was insignificant and, thus, the grain size remained at 29 µm, as shown in Figure 3.3. On the other hand, the recrystallization depth was strongly affected by the heat-flux irradiation time.

The cross sectional SEM images of the thermally irradiated W targets in Figure 3.4 show that the recrystallization layer consists of new grains with a specific thickness. Further, the interior temperature of the target decreased as the distance from the target surface increased. The thickness of the recrystallization layer was finite near the surface, but it increased in response to the total transferred energy. For a transferred energy of 1,157 MJ/m², the recrystallization layer extended to a depth of 1.7 mm. The recrystallization layer thickness increased to 2.6 mm at a higher transferred energy and longer irradiation time (1,729 MJm² and 300 s, respectively). At the highest transferred energy and longest irradiation time, 2,496 MJ/m² and 420 s, respectively, recrystallization occurred at depths of up to 3 mm within the tungsten target.

In summary, the recrystallization layer thickness varies with the irradiation time. With sufficient irradiation time, recrystallization occurs at deeper positions within the target, despite the low temperature and the low mobility of the grain boundary migration. The grain boundary mobility tends to decrease in accordance with the Arrhenius relation as the temperature decreases [36]. Hence, the required irradiation

time must be increased exponentially for deeper recrystallization to occur within the tungsten targets, which are maintained at lower temperatures. Therefore, it can be deduced that the recrystallization thickness becomes saturated at a specific value for a longer irradiation time and larger transferred thermal energy, as shown in Figure 3.5.

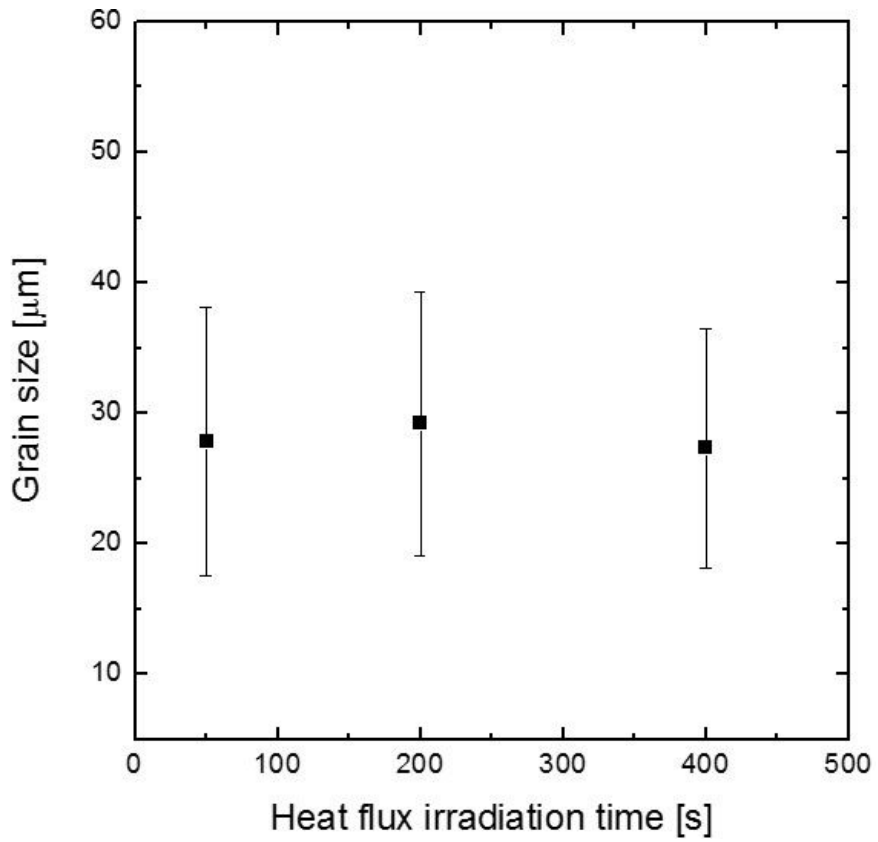


Figure 3.3 Grain size variation according to heat flux irradiation time

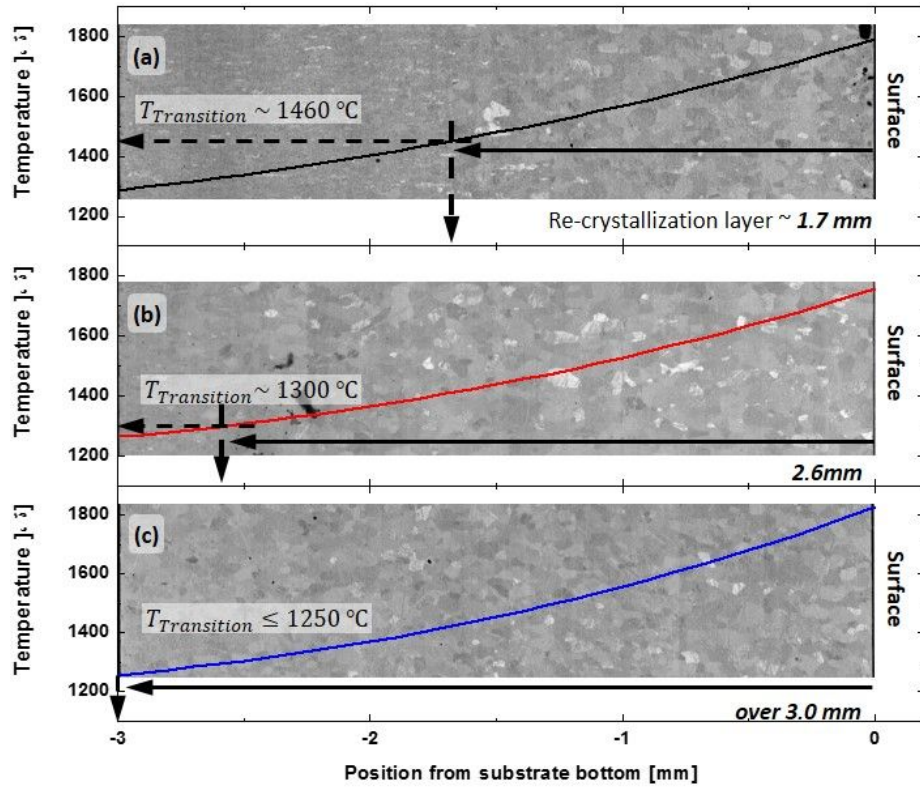


Figure 3.4 Thickness variations of recrystallized layer according to the heat flux irradiation time

(a) 180 s, $T = 1758 \text{ } ^\circ\text{C}$ with 1157 MJ/m^2 (6.4 MW/m^2)

(b) 300 s, $T = 1825 \text{ } ^\circ\text{C}$ with 1729 MJ/m^2 (5.8 MW/m^2)

(c) 420 s, $T = 1791 \text{ } ^\circ\text{C}$ with 2496 MJ/m^2 (5.9 MW/m^2)

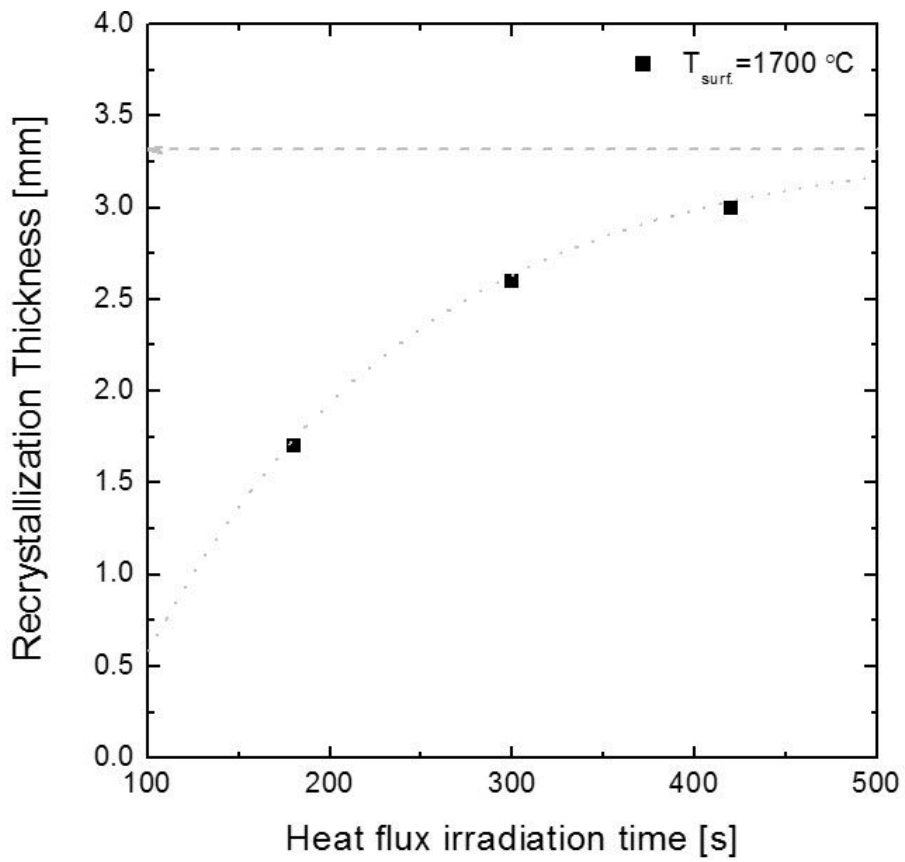


Figure 3.5 Recrystallization thickness according to heat flux irradiation time

3.2 Recrystallization characteristics of different tungsten types

To understand the effect of the initial grain structure on the recrystallization of the tungsten target, heat-flux irradiation of the three tungsten target types, KW-v, KW-r, and PW-h, was conducted. The two rolled tungsten targets exhibit the same recrystallization characteristics; thus, only two types, KW-v and PW-h, are discussed below. The PW-h and KW-v tungsten targets were thermally irradiated under similar heat flux, surface temperature, and irradiation time conditions of approximately 5 MWm^{-2} , $1,700 \text{ }^\circ\text{C}$, and 200 s , respectively. Figure 3.6 shows the grain orientation maps and grain boundary misorientation angle distributions for the PW-h and KW-v targets. The recrystallized surface of KW-v exhibits an increased average grain size of $20.1 \text{ }\mu\text{m}$, which is relatively smaller than that of PW-h. From the grain boundary misorientation angle distribution of KW-v, it can be seen that a large number of sub-grains with misorientation angles lower than 15° remain on the recrystallized surface. The sub-grains are primarily distributed between the large grains with high angle boundaries and grains with different orientations. The low angle boundaries that surround the sub-grains may be a weak point, because a low angle boundary is composed of arrays of dislocations.

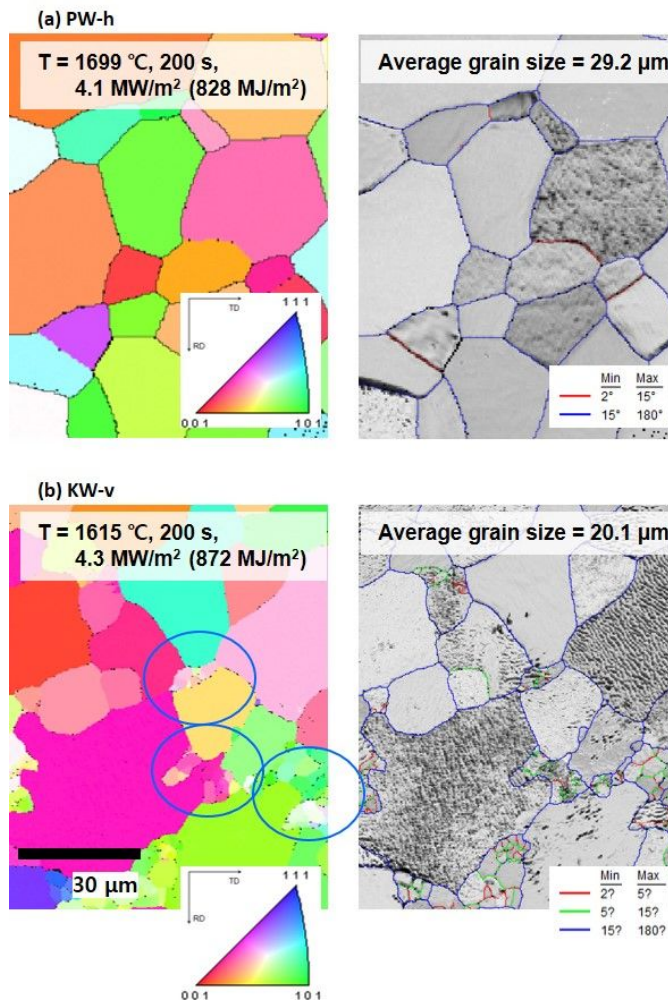


Figure 3.6 Grain Structure Change of Different Tungsten Type

(a) PW-h heat flux irradiated in 1699 °C, 200 s and 4.1 MW/m² (828 MJ/m²)

(b) KW-v heat flux irradiated in = 1615 °C, 200 s and 4.3 MW/m² (872 MJ/m²)

3.3 Defects rearrangement during the recrystallization

The cross sectional SEM images (Figure 3.7), which were created using focused ion beam (FIB) etching, show the internal structures of the recrystallized grains of the PW-h and KW-v targets. The PW-h target has no defects within and at the grain boundaries, and the defects are not prominently gathered at a specific position. However, the KW-v target exhibits strongly accumulated defects in a specific area. The initial defects, which were produced during the manufacturing process (e.g., swaging) and are randomly distributed in the target, migrate to the sub-grain boundaries as shown in Figure 3.7 (b). The migrated defects, such as dislocation and vacancy, accumulate near the sub-grain boundaries, and the gathering of these defects forms voids with sizes on the nanometer scale. These voids are also concentrated on the sub-grain boundaries. Linking of the generated voids then creates cracks on the micrometer scale at the sub-grain boundaries. These voids and cracks are the accumulation sites of retained deuterium ions and the seeds of incremental damage on the target surface.

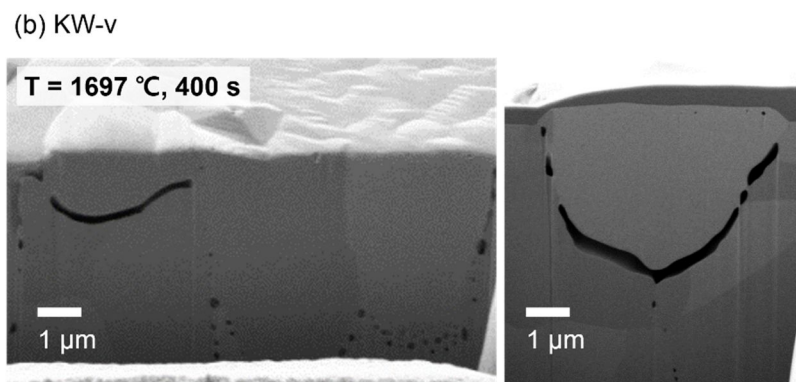
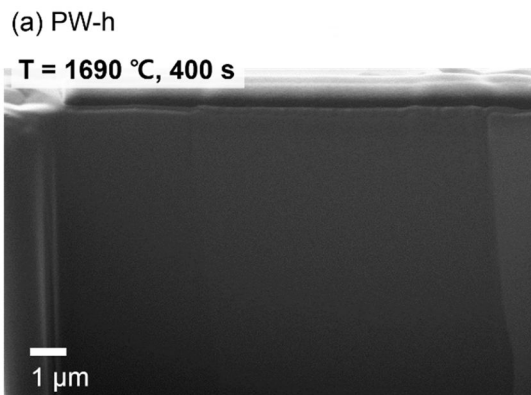


Figure 3.7 Inside damages of different type W during Recrystallization

(a) PW-h heat flux irradiated in 1690 °C, 200 s

(b) KW-v heat flux irradiated in = 1697 °C, 400 s

Chapter 4

Particle-Driven Target Surface Damage

4.1 Blister generation on different tungsten target types

The incident deuterium ions create blisters of various shapes and sizes on the target surfaces. The characteristics of the generated blisters are primarily determined not by the irradiating deuterium-ion features, but by the target characteristics. In particular, the characteristics of the near-surface grains play an important role in determining the blister types generated on the target surface. As shown in Figure 4.1, the generated blisters exhibit different characteristics on the ion-irradiated surfaces of the KW-v and PW-h targets, which have vertically and horizontally elongated grains, respectively. On the surface of the KW-v target, only blisters that are less than 1 μm in diameter are observed following deuterium-ion irradiation. These small blisters have a dome shape with relatively large height and shallow thickness of approximately 100 nm, as shown in Figure 4.2 (a), which is a cross sectional image obtained using FIB-aided FESEM. In contrast, larger blisters exist on the surface of the ion-irradiated PW-h target, and it is possible to distinguish between medium and large blisters, which are 1 – 2 μm and > 2 μm in diameter, respectively. From the cross sectional image of the medium and large blisters shown in Figure 4.2 (b), it can be seen that the medium blisters have terrace

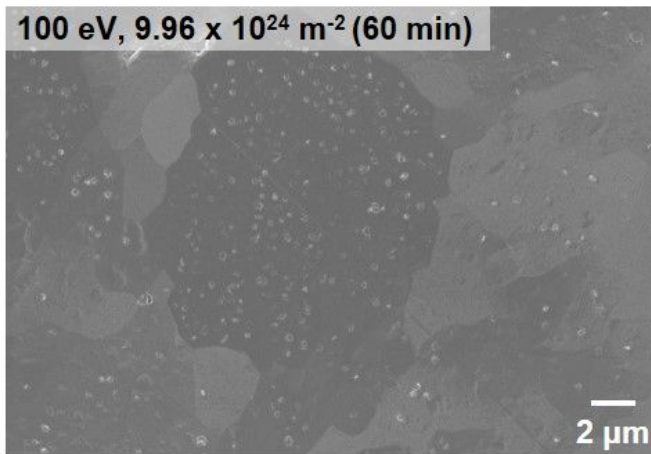
shapes, with flat tops and thicknesses of a few hundreds of nanometers. The large blisters have irregular shapes that are determined by the grain size and have thicknesses in the order of a few micrometers. From these results, it is possible to categorize the blisters into three types based on their lateral sizes and shapes: small dome-shaped blisters, medium terrace-shaped blisters, and large irregular blisters. This classification is summarized in Table 4.1 and will be used in the subsequent description of the additional ion irradiation test results.

Table 4.1 Classification of blisters generated by deuterium ion irradiation

	Small	Medium	Large
Shape	Dome	Terrace	Irregular
Size	< 1 μm	1~2 μm	> 2 μm
KW-v	◎	×	×
PW-h	○	○	•

◎ : great many, ○ : many, ◦ : some, • : few, × : none

(a)



(b)

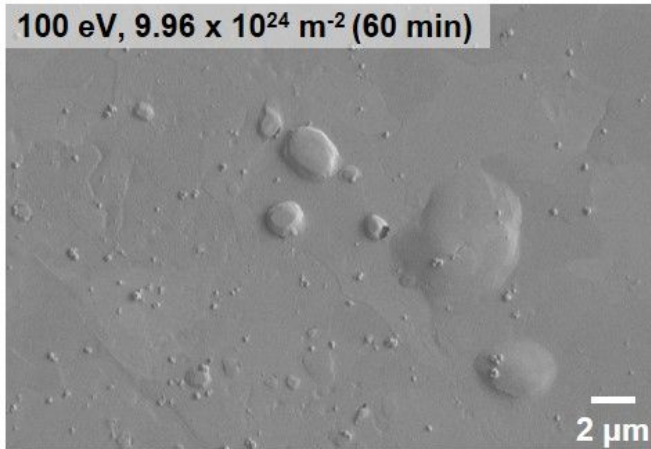


Figure 4.1 SEM image of blisters on surface of deuterium ion irradiated

(a) KW-v and (b) PW-h targets

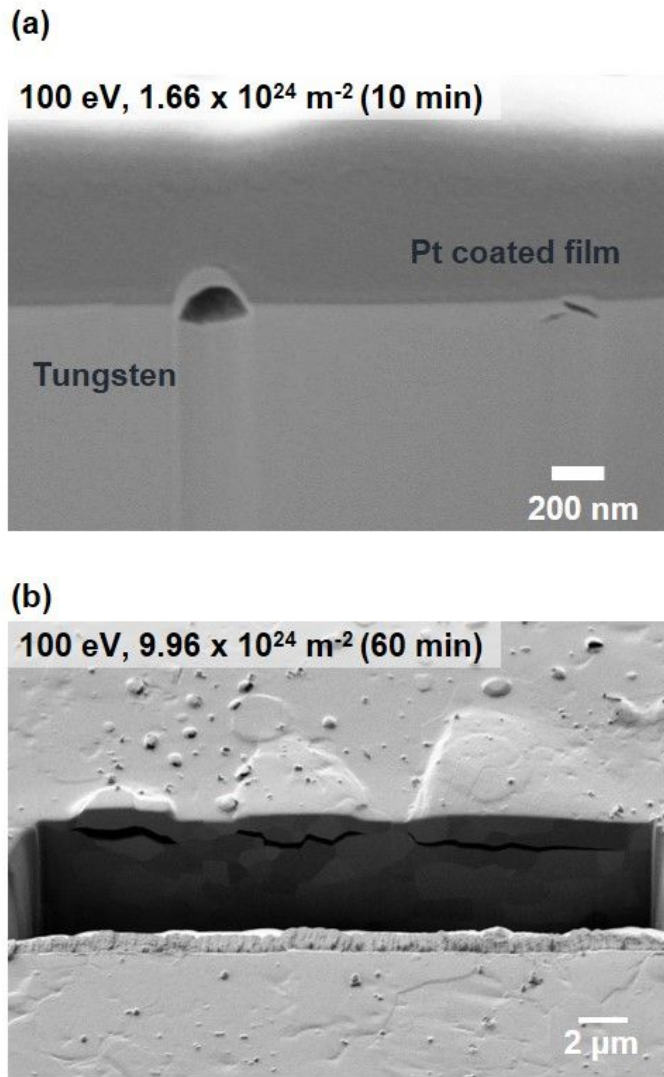


Figure 4.2 Cross sectional SEM images of (a) small blister on ion irradiated KW-v and (b) medium and large blisters on ion irradiated PW-h

4.2 Characteristics of small blisters on the target with vertically elongated grain

4.2.1 Small dome-shaped blister generation

Small blisters are generated by deuterium-ion irradiation on the surfaces of both targets (KW-v and PW-h). In particular, the deuterium-ion-irradiated KW-v target has small blisters only. Thus, the characteristics of the small blisters were examined using the deuterium-ion-irradiated KW-v target. Typical small blisters are represented in Figure 4.3, which is a SEM image of the deuterium-ion-irradiated KW-v target under 100 eV impact energy and $1.66 \times 10^{24} \text{ m}^{-2}$ fluence over a 10-min irradiation time. Small blisters have dome shapes of a few hundreds of nm in size, and a high number density of a few blisters per μm^2 in the blister reach region. From results of the EBSD analysis on the deuterium-ion-irradiated target surface, it is apparent that the small dome-shaped blisters are most pronounced in the specific region with $\langle 111 \rangle$ grain orientation and have lowest density in the area with a grain orientation of $\langle 001 \rangle$, as can be seen in Figure 4.4 The grains oriented in the $\langle 111 \rangle$ direction have the coarsest distribution of tungsten atoms, and this facilitates deuterium-ion penetration.

The blister generation mechanism due to the deuterium-ion irradiation is explained in Figure 4.5. The deuterium ions (D^+ , D_2^+ , and D_3^+) irradiate the tungsten target and the incident ions penetrate the tungsten. The deuterium ions retained within the tungsten are concentrated within defects such as vacancies and nano-voids, as shown in Figure 4.5 (a). As can be seen in Figure 4.5 (b), the trapped ions recombine with neighboring ions and create deuterium gas at the defect sites. The pressure of the deuterium gas then further expands the deuterium accumulation sites. Additional

deuterium gas accumulates with increased deuterium fluence, i.e., increases in the total number of incident deuterium ions in the unit area. Large amounts of deuterium gas can cause internal voids in the target to expand, as shown in Figure 4.5 (c). In addition, further irradiation by deuterium ions can eradicate small dome-shaped blisters, by causing them to burst at the side edge, as shown in Figure 4.5 (d). The deuterium gas retained within these blisters is released into the plasma when the blisters burst [45]. This blister destruction mechanism is discussed in chapter 4.4.1, when the blister bursting is examined in greater detail.

Figure 4.6 shows the structure of a small dome-shaped blister as observed using FIB cross sectioning. The blister has a thick top (90 nm thick) and a thin side wall (50 nm thick). A deuterium-gas-filled space is created at the blister position that has a depth of 70 nm from the top surface of the target. The blister is, therefore, a plastic deformation.

100 eV, $1.66 \times 10^{24} \text{ m}^{-2}$ (10 min)

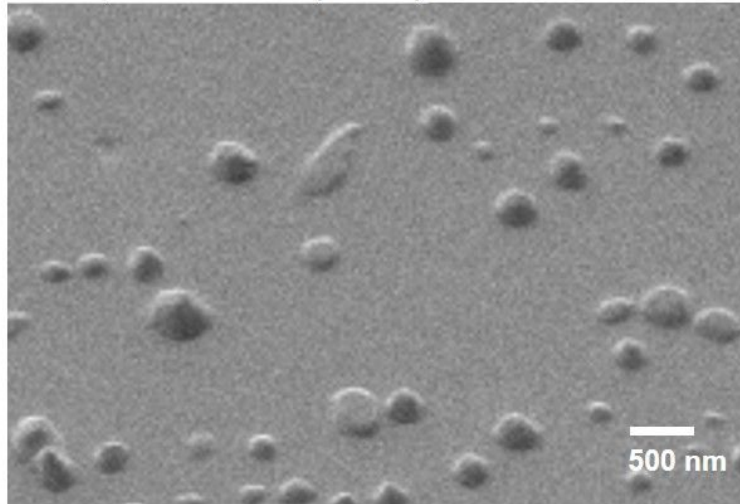


Figure 4.3 Blister generation by ion flux irradiation with conditions of 100 eV and $1.66 \times 10^{24} \text{ m}^{-2}$ (10 min)

100 eV, $8.30 \times 10^{23} \text{ m}^{-2}$ (5 min)

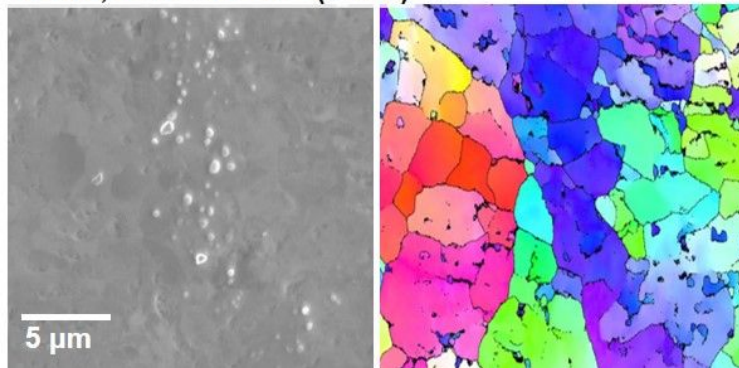


Figure 4.4 Generation characteristics of small blister with conditions of 100 eV and $8.30 \times 10^{23} \text{ m}^{-2}$ (5 min)

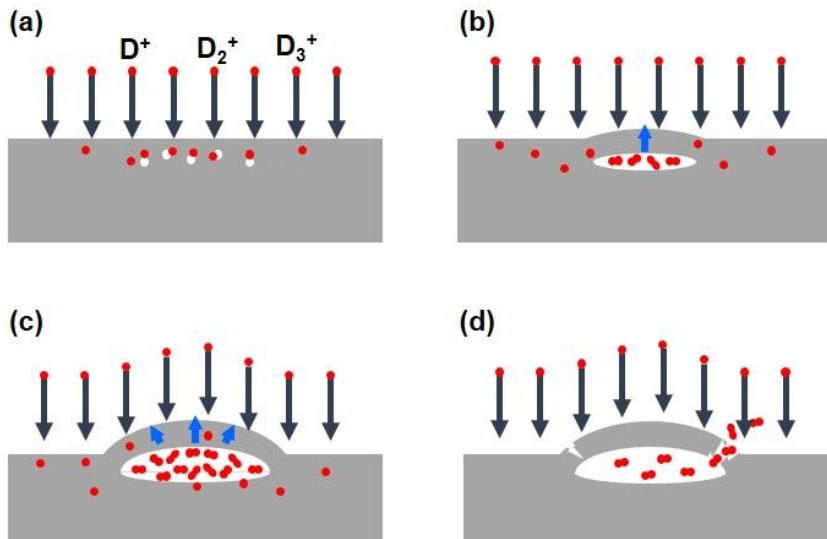


Figure 4.5 Sequential diagram of small dome-shaped blister generation by deuterium ion irradiation

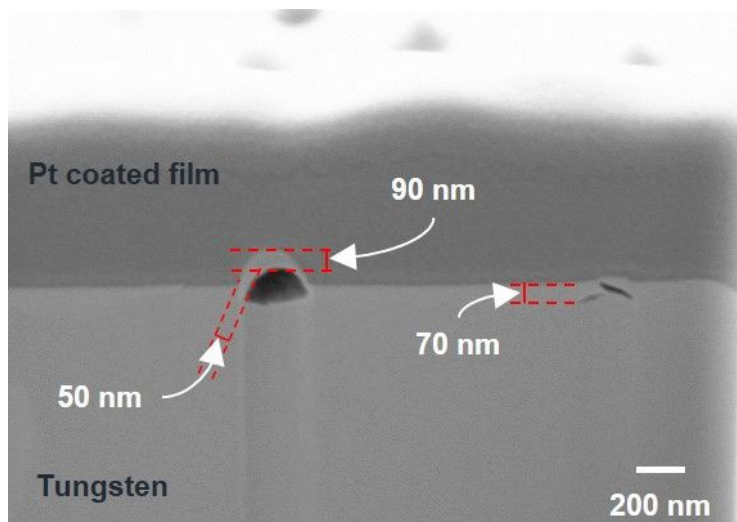


Figure 4.6 Cross sectional SEM image of small dome-shaped blister

4.2.2 Characteristics of small dome-shaped blister with irradiation conditions

In order to understand the characteristics of small dome-shaped blisters, the KW-v tungsten target was irradiated under various irradiation-time and deuterium-ion incident energy conditions. An increase in irradiation time means that a greater number of deuterium ions collide with the tungsten target, so the fluence and total transferred energy is increased along with the irradiation time. Figure 4.7 shows the resultant variations in the blister characteristics, i.e., number density, size, and evolution phase. At a relatively low fluence (i.e., at the beginning of the irradiation phase), the blisters are sufficiently generated and grown, as can be seen in Figure 4.7 (a). At higher fluence, the blisters increase in terms of both lateral size and number density, as can be seen in Figure 4.7 (b) - (d). However, because of the limited surface area, the blister lateral size tends to saturate at certain values, as shown in Figure 4.8. At 6.02×10^{24} #/m² fluence, the blister growth ceases as a result of bursting. At 1.19×10^{25} #/m² fluence, the blister size is maintained, but the number density is increased. The next condition, which is 2.38×10^{25} #/m² fluence, eradicates all of the blisters. Only traces of blisters and small structures located at the blister centers are found. This means that full bursting of the blisters has occurred, as shown in Figure 4.7 (e).

The deuterium-ion incident energy is a key parameter influencing the small dome-shaped blister characteristics. Figure 4.9 shows SEM images of blisters generated by deuterium ions with incident energies of 50, 100, and 200 eV. At an incident energy of 50 eV, the generated blisters have over 500 nm lateral size and a lower number density while, at an incident energy of 100 eV, the blister lateral size is reduced and the number density is increased. The blister lateral size and number density are not changed by increasing the incident energy to 200 eV, as can be seen in Figure 4.10. The behavior

most sensitive to the changes in the incident energy is the blister bursting. The 50 eV deuterium-ion irradiation does not cause blisters to form on the irradiated surface. However, as the incident energy increases, the burst area of the blisters is also enlarged. These results suggest that blister bursting may be analyzed using sputtering enhancement.

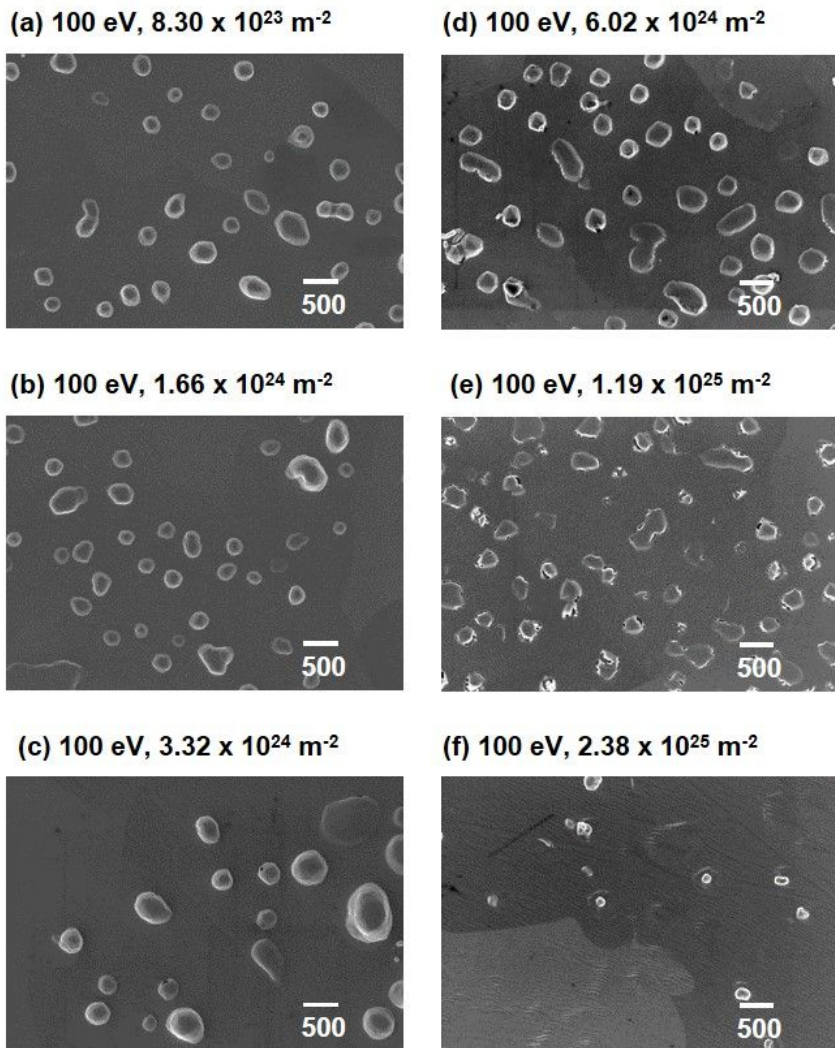


Figure 4.7 Character of small blister according to increment of ion fluence

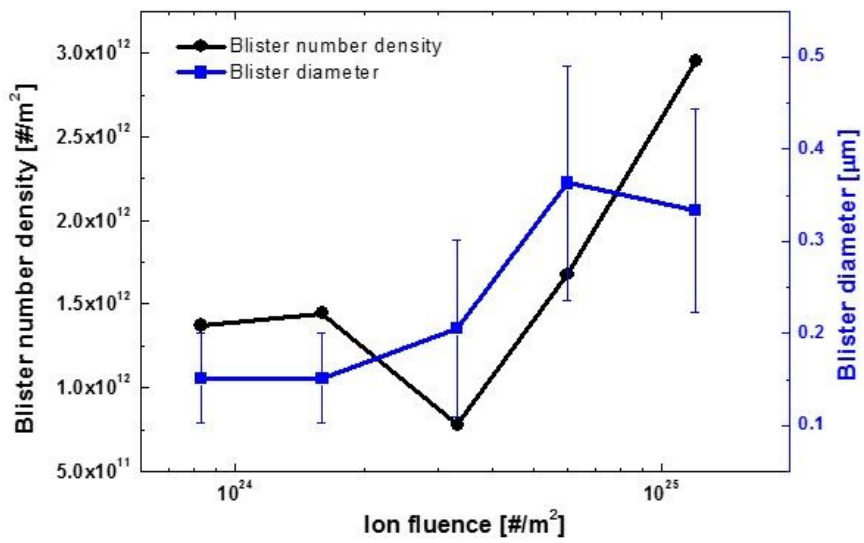


Figure 4.8 Size and number density of small blister according to ion fluence

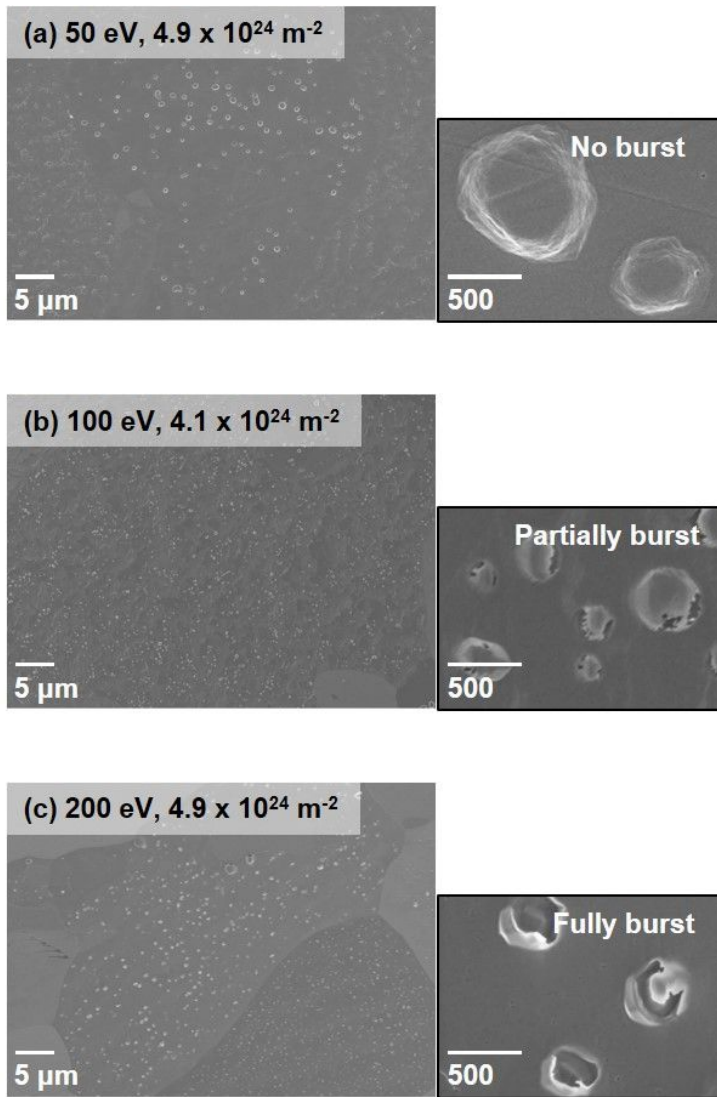


Figure 4.9 Character of small blister according to ion energy

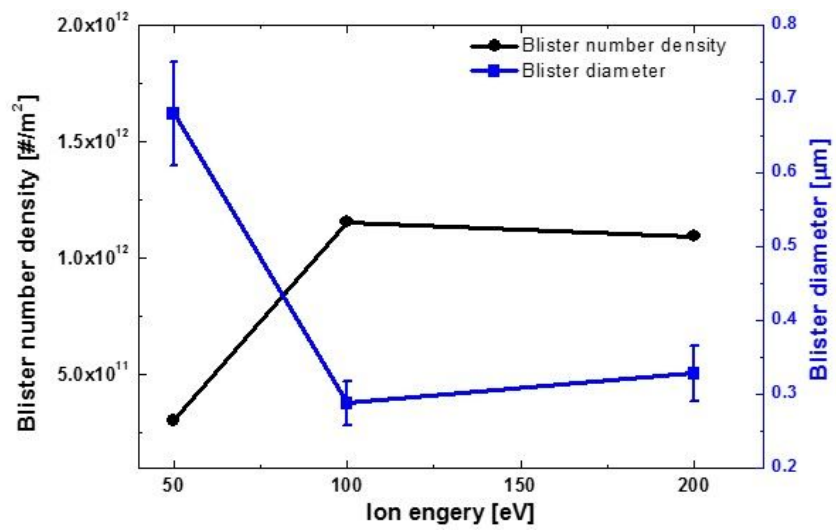


Figure 4.10 Size and number density of small blister according to ion fluence

4.3 Characteristics of medium terrace-shaped and large irregular-shaped blisters on the target surface with horizontally elongated grain

4.3.1 Generation of medium and large blisters

The medium and large blisters are generated on the surfaces of the horizontally elongated grain targets (PW-h and KW-h) only. Both kinds of tungsten targets (which have similar grain characteristics) exhibit the same results regarding the generation of medium and large blisters and, thus, the purity difference of 0.03 %p between PW-h and KW-h does not play an important role in the generation of these blisters. Therefore, the results for the PW-h target are primarily discussed in this chapter.

As shown in Figure 4.11, the medium blister has a terrace shape with a flat top and a steeply inclined side. In contrast, the large blisters are irregularly shaped and have moderately sloped sides. The average sizes of the medium terrace-shaped and large irregular-shaped blisters are of the order of micrometers and a few micrometers, respectively, with respective number densities of a few tens of thousands and a few thousands per square millimeter. From the cross sectional image of the medium terrace-shaped and large irregular-shaped blisters given in Figure 4.12, it can be seen that the medium terrace-shaped blister has a thickness of 0.9 μm , while the large irregular-shaped blister has a slightly larger thickness of approximately 1.3 μm . Both blisters have underlying cracks that occurred along a grain boundary. Because of the horizontally elongated grains of the PW-h and kW-h targets, the grain boundaries are in close proximity along the surface. These grain boundaries act as defects that can trap the retained deuterium ions and cause deuterium-ion recombination. Gas-phase

deuterium is then produced and concentrated at grain boundaries, as in the case of the small dome-shaped blisters, which was shown in Figure 4.5 (b) and (c) of section 4.2.1. Because the medium terrace-shaped and large irregular-shaped blisters are generated from the same kind of defect – a grain boundary, both blister types have similar thicknesses, which are determined by the existing depth of the source grain boundary from the target surface.

At the beginning of the blister generation phase, the characteristics of the formed crack and the grain orientation determine the blister type. The size of the initial generated crack is increased by the gas-phase deuterium that accumulates in the crack. At that moment, a slip can occur in a specific grain which has a relatively large size and satisfies the required plane and direction conditions for slip systems, such as those of a low-indexed $\{110\}\langle 111 \rangle$ or higher-indexed slip system [12, 39]. The occurrence of a slip expands the crack in the vertical direction and creates a large cavity, as illustrated in Figure 4.13 (a). Through the cracking and slip formation, a medium terrace-shaped blister is generated on a target surface that has a horizontally elongated grain. In contrast, if the horizontal expansion of the initial crack is not limited by a slip, the crack grows horizontally across the grain boundaries. This inter-grain crack leads to the formation of a large irregular-shaped blister, as shown in Figure 4.13 (b).

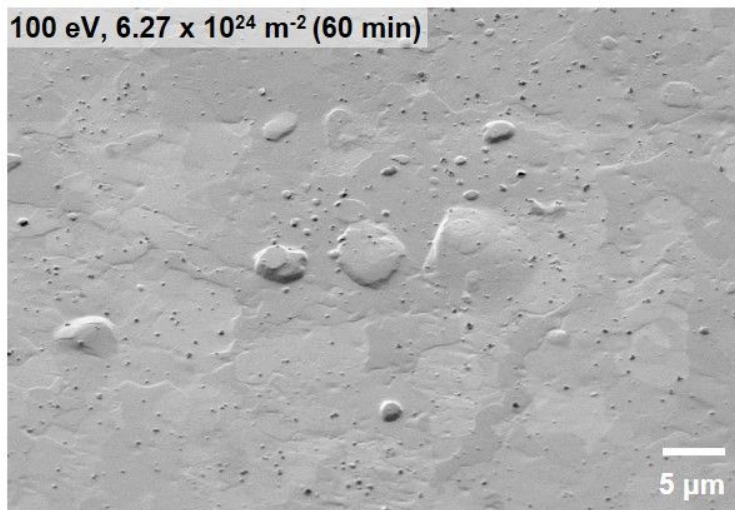


**Figure 4.11 Medium terrace-shaped and large irregular-shaped blisters
on the deuterium ion irradiated tungsten target with horizontally elongated grains**

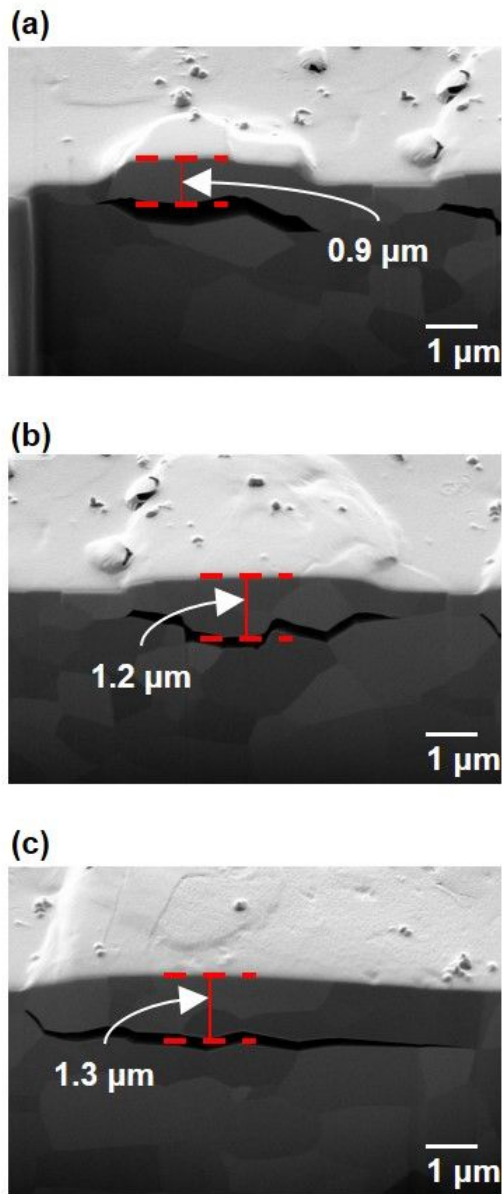


Figure 4.12 Cross sectional SEM images of (a) medium terrace-shaped blister, (b) and (c) large irregular-shaped blister

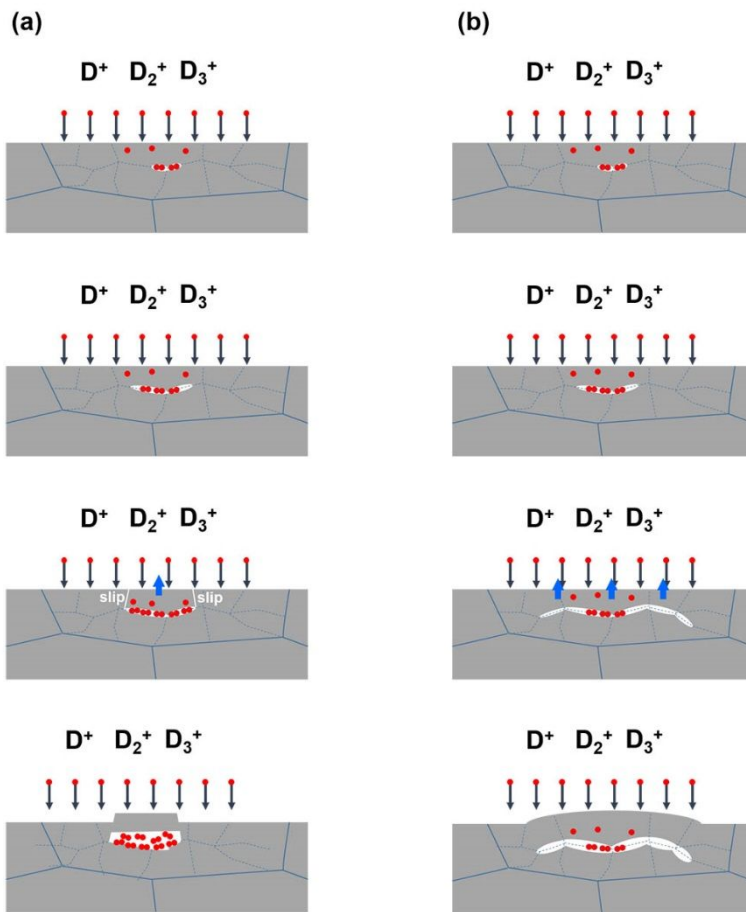


Figure 4.13 Schematic diagram of (a) medium terrace-shaped blister generation

(b) large irregular-shaped blister generation

4.3.2 Characteristics of medium and large blisters depending on irradiation conditions

To understand the characteristics of the medium terrace-shaped and large irregular-shaped blisters, the PW-h target (which has a horizontally elongated grain) was irradiated by deuterium ions under various irradiation-time and deuterium-ion incident energy conditions. As the irradiation time increases, a larger amount of deuterium ions impact on the surface of PW-h target and the fluence and total transferred energy increase. Figure 4.14 shows the variations in the medium terrace-shaped and large irregular-shaped blister characteristics according to changes in the deuterium-ion irradiation period. The blisters are enlarged and the blister number density is increased under longer irradiation conditions. As indicated quantitatively in Figure 4.15, the diameter of the large irregular blister changed significantly, from 2.5 to 4.5 μm , because of the accumulation of a larger amount of gas-phase deuterium. In contrast, the blister number density is reduced with increased irradiation time. In particular, the number density of the medium terrace-shaped blisters is reduced remarkably, as a result of the increased sputtering effects. The relatively smaller medium blisters are burst completely and disappear, leaving only the aforementioned trace. The relatively larger medium blisters are still present but are partially burst. Therefore, the number density of the medium terrace-shaped blisters decreases over longer irradiation time.

As shown in Figure 4.16, the PW-h target is irradiated by deuterium ions with incident energy conditions of 50 – 200 eV. Under the lowest impact energy conditions, all three blister types exist. The small dome-shaped blister characteristics are affected by the impact ion energy as has been explained in chapter 4.2.2. The medium terrace-shaped and large irregular-shaped blisters exhibit decreased blister size and increased

number density in response to increased incident deuterium-ion energy. In particular, the reduction in size of the large irregular-shaped blisters is most prominent, as shown in Figure 4.17. Under low-energy conditions of 50 eV, the large irregular-shaped blister is approximately 6.9 μm in size. As the incident ion energy is increased, the size is reduced to approximately 3 μm because of the reduced gas pressure within the blister. This is due to a reduction in the trapped deuterium near the surface. Higher incident ion energy conditions lead to a higher surface temperature due to a larger energy transfer to the surface. In this case, more deuterium is retained and can be diffused to a greater depth within the tungsten target, due to the increase in the diffusion coefficient [55]. Therefore, the reduced deuterium trapping near the surface reduces the internal blister pressure and causes the large irregular-shaped blisters to decrease in size. In contrast, the medium terrace-shaped blisters are less affected by increased deuterium diffusion, because the occurrence of a slip inside the grain as well as internal gas pressure are the key parameters affecting the generation of these blisters. As regards the blister number density, an increase in the number of medium terrace-shaped blisters is apparent in Figure 4.17. The high-energy condition provides an advantageous environment for the occurrence of slipping. Thus, the generation of medium terrace-shaped blisters increases, despite the decreased gas pressure near the surface of the tungsten target.

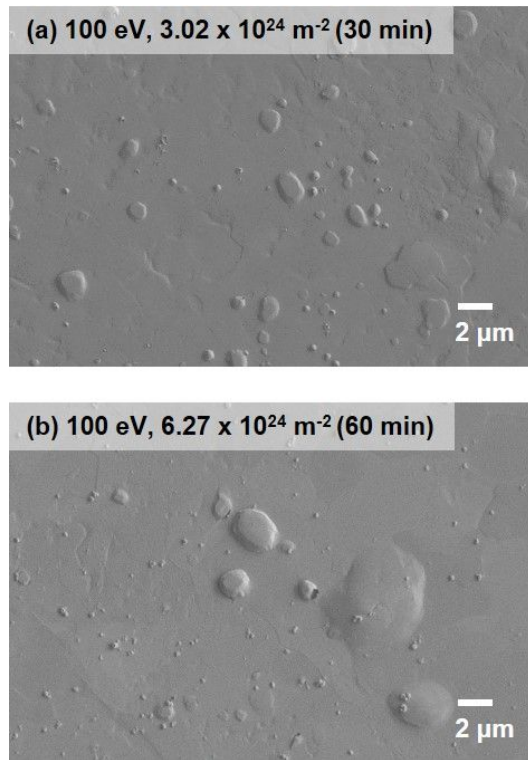


Figure 4.14 SEM images of medium terrace-shaped and large irregular-shaped blisters with

(a) $3.02 \times 10^{24} \text{ m}^{-2}$ of fluence condition (100 eV, 30 min) and

(b) $6.27 \times 10^{24} \text{ m}^{-2}$ of fluence condition (100 eV, 60 min)

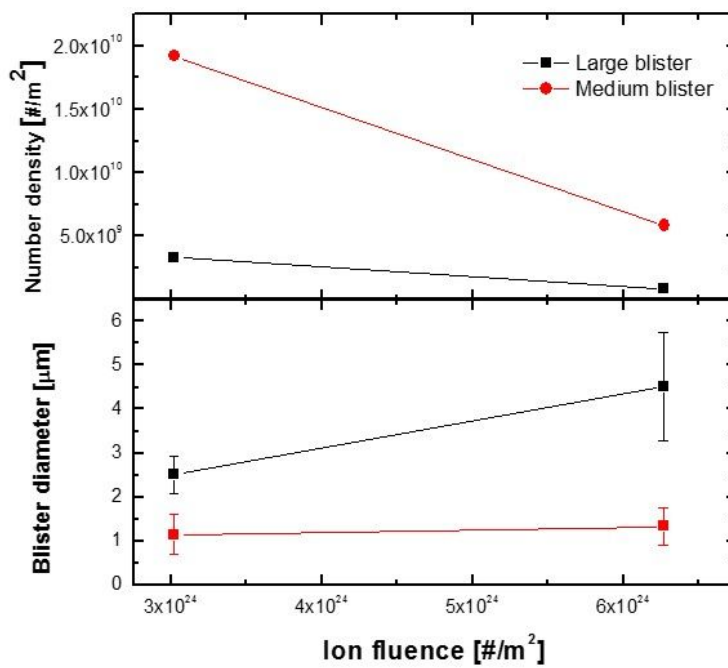


Figure 4.15 Size and number density variations of medium terrace-shaped and large irregular-shaped blisters according to incident ion fluence

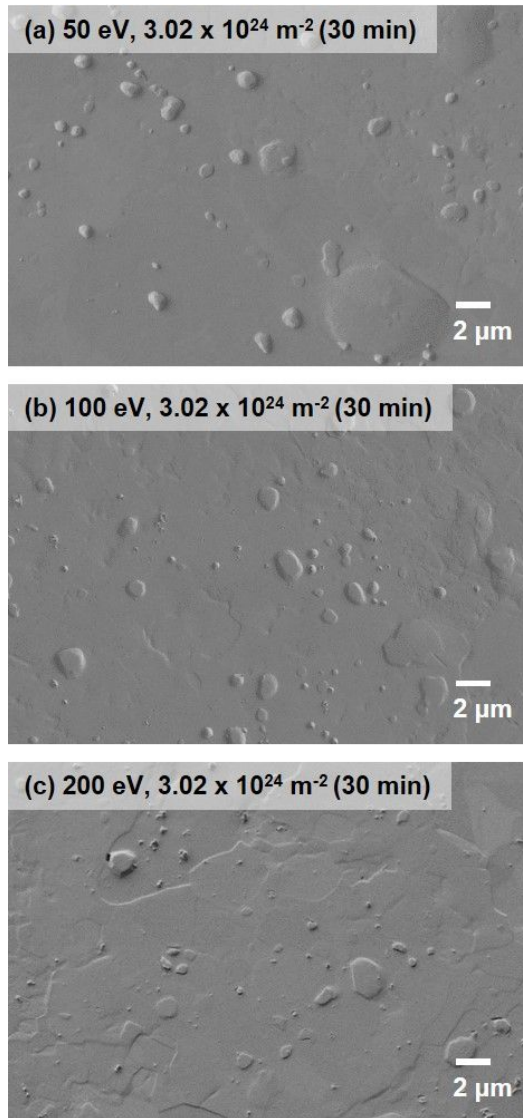


Figure 4.16 SEM images of medium terrace-shaped and large irregular-shaped blisters with

- (a) 50 eV incident energy condition ($3.02 \times 10^{24} \text{ m}^{-2}$, 30 min),
- (b) 100 eV incident energy condition ($3.02 \times 10^{24} \text{ m}^{-2}$, 30 min) and
- (c) 200 eV incident energy condition ($3.02 \times 10^{24} \text{ m}^{-2}$, 30 min)

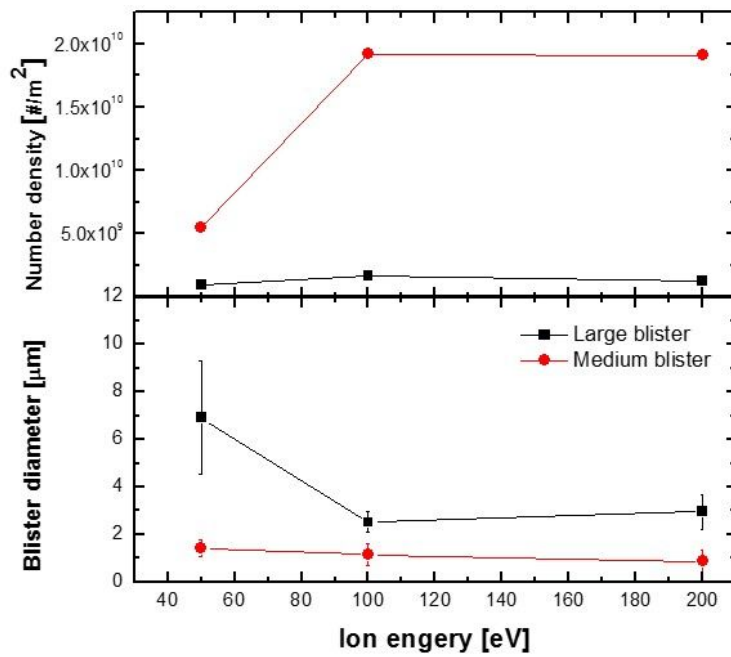


Figure 4.17 Size and number density variations of medium terrace-shaped and large irregular-shaped blisters according to incident ion energy

4.4 Destruction of blisters by sputtering aided bursting

4.4.1 Small dome-shaped blister destruction mechanism

In the literature, the destruction of generated blisters is achieved only through a thermal burst that occurs at an elevated surface temperature [45]. After surface heating to over 727 °C, the blisters are burst using various techniques such as side bursting and bursting with a partially or fully opened lid. The blister bursting is caused by increased internal gas pressure due to additional target heating, which is conducted after the deuterium-ion irradiation. Hence, the various types of blisters are burst simultaneously and each bursting shape is obtained. This mechanism for blister destruction does not yield sufficient explanation of the blister lifespan, from evolution to disappearance, in response to deuterium-ion irradiation. Therefore, sputtering, which is based on a basic principle of particle impact as well as the application of an elevated temperature, is a key tool that can increase the understanding of blister bursting, especially under elevated incident energy conditions. In this section, the blister bursting by sputtering method is explained taking surface modification into account. In particular, the small dome-shaped blisters, which burst most prominently in the case of a deuterium-ion irradiated target, are first discussed. As shown in Figure 4.18, the small dome-shaped blisters have thicker lids and thin steeply inclined side walls. Deuterium ions incident on the side wall of once such blister impact obliquely on the surface at an angle of approximately 70°. This oblique ion irradiation is the most important cause of blister bursting in response to increased sputtering. The sputtering yield is expressed as [56].

$$Y(E, \theta) = Y(E, 0) \times \left(\frac{1 + A \sin \theta}{\cos \theta} \right)^f \exp \left(-\Sigma \left(\frac{1}{\cos \theta} - 1 \right) \right) \quad (4.1)$$

where θ and E are the incident angle and energy of the ion, respectively. $Y(E_i, \theta)$ is the sputtering yield at incident conditions of θ and E , and A , f , and Σ are calculated considering an atomic collision with inter-atomic potential and energy loss [56]. The sputtering yield is calculated for D_3^+ ions, as this is the most effective ion species in terms of tungsten sputtering. The results of this calculation are shown in Figure 4.19, and it is apparent that the calculated sputtering yield has a maximum value at an angle of 70° . The sputtering yield obtained at 70° is 25 times greater than that of the normal incident ion case. The point on the blister side wall that satisfies an incident angle of 70° is therefore the most easily sputtered. In addition, the side of the blister is thinner than the other parts. Therefore, the blister side wall is its weakest point as regards withstanding the internal pressure of the blister. Hence, the blister bursting begins at the side wall of the small dome-shaped blister, initiated by increased sputtering and internal pressure. After the bursting is initiated, the sputtering is continued at the near point of the blister side wall satisfying the incident angle requirement of 70° , as illustrated in Figure 4.20. When the entire blister side wall is sputtered with incident deuterium ions, the lid of the blister is opened and finally separated from the blister body. Figure 4.21 shows the complete small dome-shaped blister destruction process. After the separation of the blister lid, the remaining blister parts are retained in varying to specific shapes. This will be studied in future work.

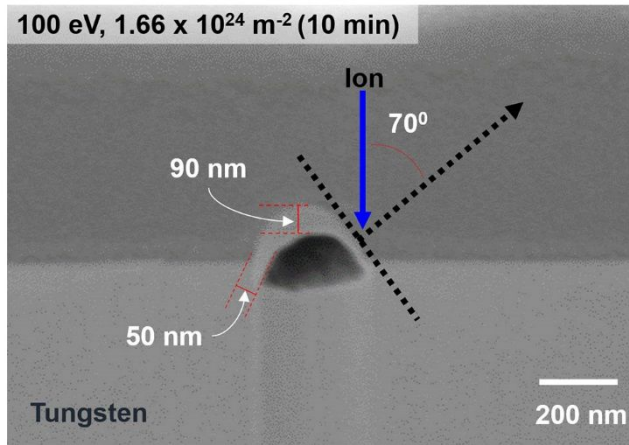


Figure 4.18 Incident angle of deuterium ion to side wall of small dome-shaped blister

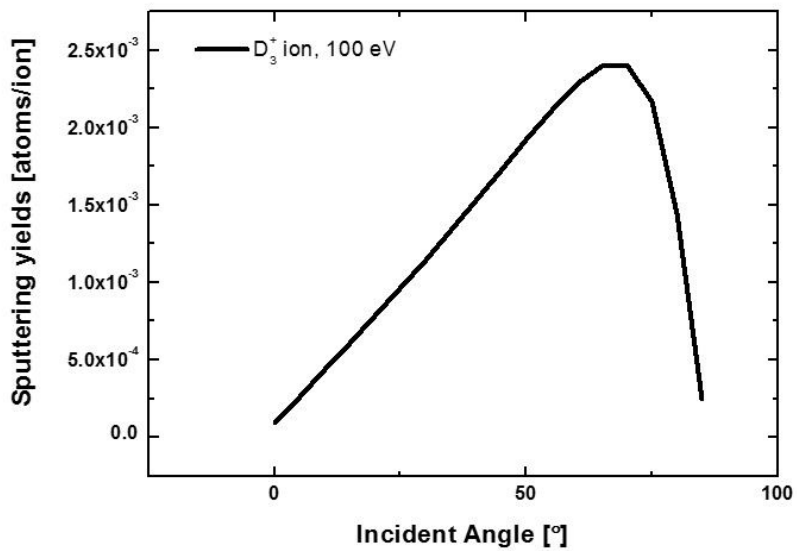


Figure 4.19 Local angle effect for sputtering on the blister surface

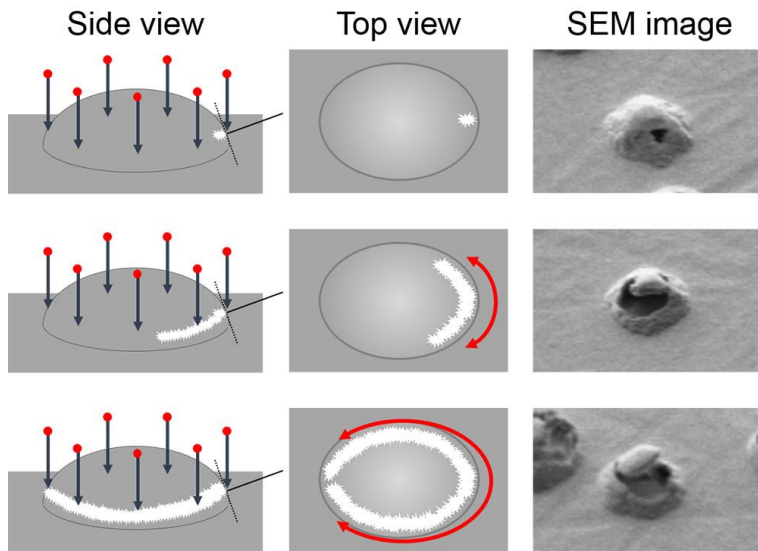


Figure 4.20 Sequential diagram of blister destruction with sputtering aided bursting

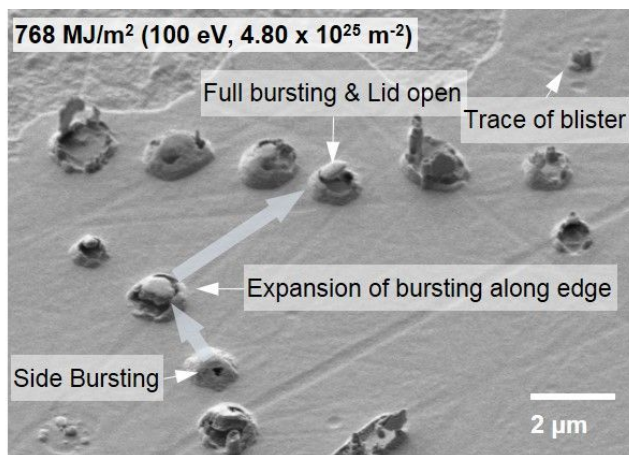


Figure 4.21 Surface SEM image of blister destruction procedure with sputtering aided bursting

4.4.2 Destruction of medium terrace-shaped blisters

The destruction mechanism using sputtering-aided blister bursting can also be applied to medium terrace-shaped blisters. The sputtering is directed at the side wall of the medium terrace-shaped blister, which is stiffly inclined as shown in Figure 4.22. The medium terrace-shaped blister has a narrower area that satisfies the 70° incident angle requirement, and a thicker side wall than that of small dome-shaped blister. Full destruction with top opening rarely occurs for medium terrace-shaped blisters, even for long irradiation times of 60 min and under high energy conditions of 200 eV, which cause full destruction of small dome-shaped blisters. On the other hand, since the large irregular-shaped blisters have no areas that satisfy the incident angle of 70° requirement, increased sputtering does not occur on large blister surfaces.

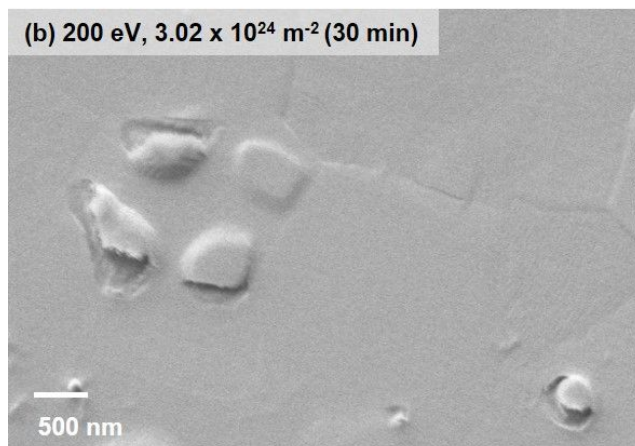
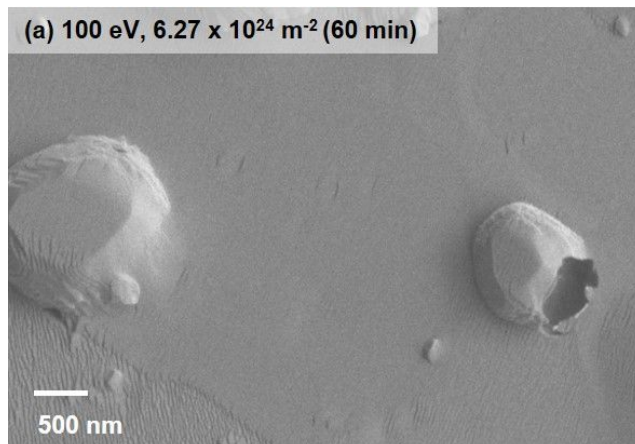


Figure 4.22 Surface SEM images of partially destroyed medium terrace-shaped blister with irradiation conditions of (a) 100 eV, $6.27 \times 10^{24} \text{ m}^{-2}$ (60 min) and (b) 200 eV, $3.02 \times 10^{24} \text{ m}^{-2}$ (30 min)

Chapter 5

Aggravation of Pre-Generated Damage on

Tungsten Surface by Additional Thermal and

Particle Flux

5.1 Thermally pre-irradiated tungsten damage aggravation by deuterium-ion irradiation

5.1.1 Ion flux irradiation on recrystallized tungsten

To understand thermally generated damage aggravation on tungsten targets, deuterium-ion irradiation of the recrystallized surface was conducted using heat-flux irradiation. Two tungsten target types (KW-v and PW-h) were pre-irradiated using a heat flux of approximately 5 MWm^{-2} with a surface temperature of $1,700 \text{ }^{\circ}\text{C}$. The irradiation time was varied from 50 – 400 s. All targets were completely recrystallized during the irradiation time and had similar grain structure characteristics. Ion irradiation of the recrystallized tungsten surface was also conducted with an incident ion energy range of 50 – 200 eV and the same fluence of $3.5 \times 10^{24} \text{ \#/m}^2$. These

irradiation conditions are summarized in Table 5.1

Table 5.1 Conditions of pre-heat flux irradiation and aggravation by deuterium ion irradiation

Type	Heat flux irradiation			Ion flux irradiation	
	T_{surface} [°C]	q [MW/m ²]	Irradiation time [s]	Incident energy [eV]	Fluence [#/m ²]
KW-v	1700	4-5	50-400	50-200	$\sim 10^{24}$
PW-h	1700	4-5	50-400	50-200	$\sim 10^{24}$

5.1.2 Characteristics of aggravated damage of thermally pre-irradiated tungsten by ion irradiation

Ion flux irradiation creates a recrystallized surface that has damage manifested in different shapes depending on the target type and heat-flux irradiation time. Figure 5.1 is an SEM image of the effects of ion flux irradiation on the KW-v target recrystallized through heat-flux irradiation. The ion irradiation creates a dent on the recrystallized KW-v surface of a few micrometers in size. Its depth is in the order of micrometers as depicted in Figure 5.2 which is a cross-sectional FIB image. The dents are of a similar size to the sub-grains that were discussed in section 3.2. The heat-flux-irradiated KW-v has voids and cracks created as a result of concentrated defects on the sub-grain boundaries near the tungsten target surface, as previously discussed in 3.2. The near-surface damage features are important deuterium-ion recombination sites in which gas-phase deuterium is formed. A larger amount of deuterium gas accumulates at the defects as the irradiation time passes. The pressure induced by the accumulated deuterium gas causes sub-grain ejection to the plasma, as illustrated in Figure 5.3.

After the ejection of the sub-grains, the dent remains at that site.

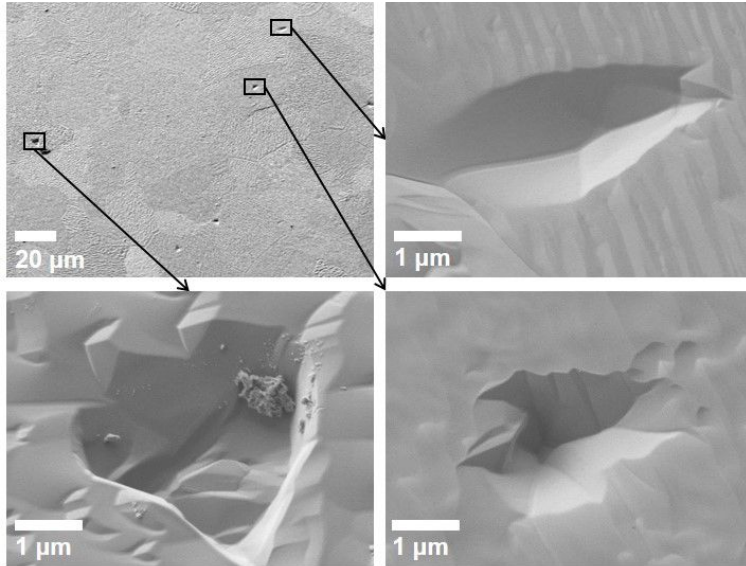


Figure 5.1 Surface SEM images of remained large dent after ejection of sub-grain

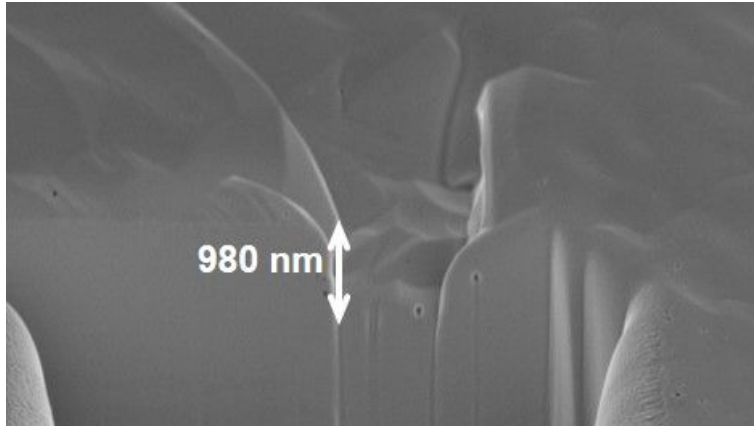


Figure 5.2 Cross-sectional SEM image of remained large dent after sub-grain ejection

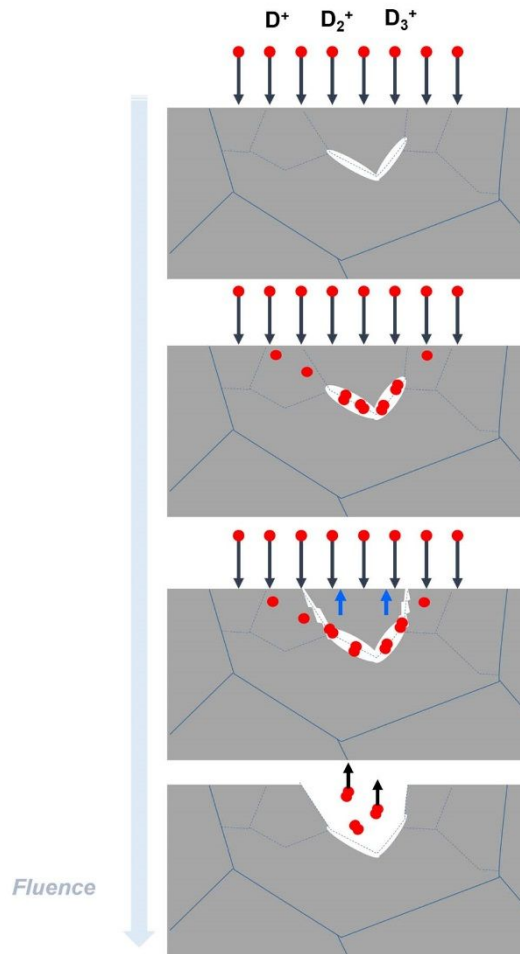


Figure 5.3 Sequential diagram for sub-grain ejection by deuterium ion irradiation on thermally pre-damaged KW-v target

The deuterium-ion irradiation of the recrystallized PW-h target surfaces causes different types of damage to those exhibited by the KW-v target. Figure 5.4 shows surface and cross sectional SEM images of the deuterium-ion-irradiated PW-h target. The surface has developed a large number of holes of less than 200 nm in size and finite depth, as depicted in Figure 5.4 (b). The bottom of each hole is the hole

generation initiation point. In the early stages of the hole generation process, deuterium ions are trapped at a defect which is positioned at the same depth as the resultant hole bottom. The trapped deuterium ions then recombine with each other and create gas-phase deuterium. Thus, the defect is expanded by the resultant gas pressure, as illustrated in Figure 5.5. As the irradiation time increases, a greater number of deuterium ions become trapped within the expanded defect area, and this increased deuterium-ion trapping creates further gas-phase deuterium. Therefore, the expanded defect develops a bubble shape that is filled with gas-phase deuterium. This phenomenon is known as hydrogen bubbling. Because of the continued irradiation, deuterium gas is supplied continuously and the pressure within the bubble increases. This lifts the upper tungsten toward the surface. At a specific pressure within the bubble, the upper layer of tungsten cannot contain the gas. The bubble destroys the upper layer of tungsten which is separated from the target surface. Therefore, a hole structure is generated. In the literature, bubble generation by hydrogen ion irradiation requires a high incident energy in the region of a few keV. This generates the defects at which accumulation then occurs [57]. However, the heat-flux-irradiated targets have concentrated defects near the surface due to the temperature gradient. Therefore, bubble generation by low-energy deuterium ions occurs easily on the recrystallized PW-h target. From Figure 5.6, which gives the results of hole size and depth measurements, the hole depth is shown to be proportional to hole size. Thus, holes with greater diameter began at positions located more deeply within the target. The hole characteristics are significantly affected by the heat-flux irradiation time, which is related to the migration of defects inside the target. At a shorter heat-flux irradiation time, the defects do not migrate to the surface sufficiently due to the reduced

temperature gradient. Thus, the holes are generated from deeper positions within the target and achieve larger sizes. As the heat-flux irradiation time increases, the hole size decreases as the hole generation begins at a relatively shallow location, as depicted in Figure 5.7.

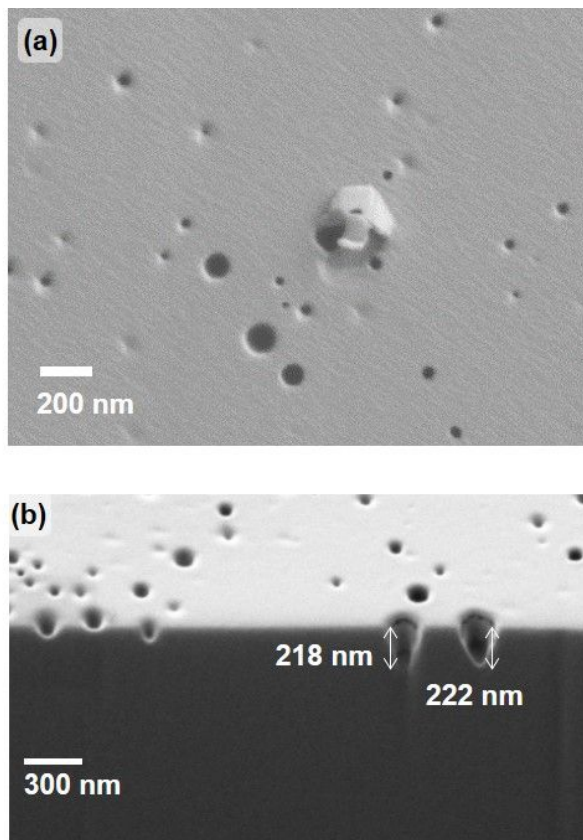


Figure 5.4 (a) Surface and (b) cross sectional SEM images of deuterium ion-irradiated PW-h targets which are pre-damaged by heat flux irradiation with $T = 1698\text{ }^{\circ}\text{C}$, 4.5 MW/m^2 , 200 s

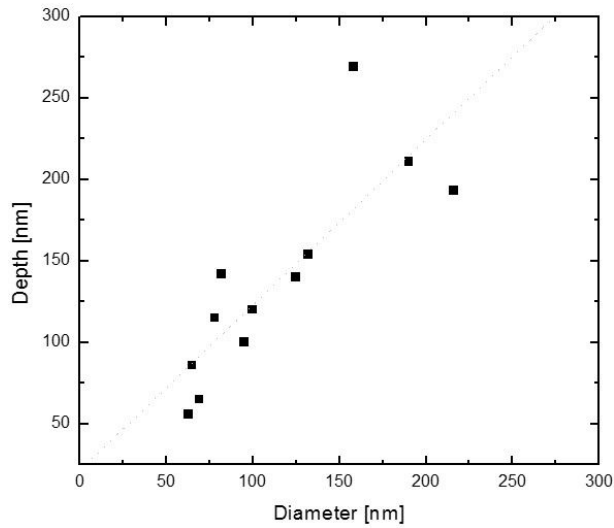


Figure 5.6 Correlation between the diameter and depth of hole structure generated by deuterium ion irradiation on thermally pre-damaged PW-h target

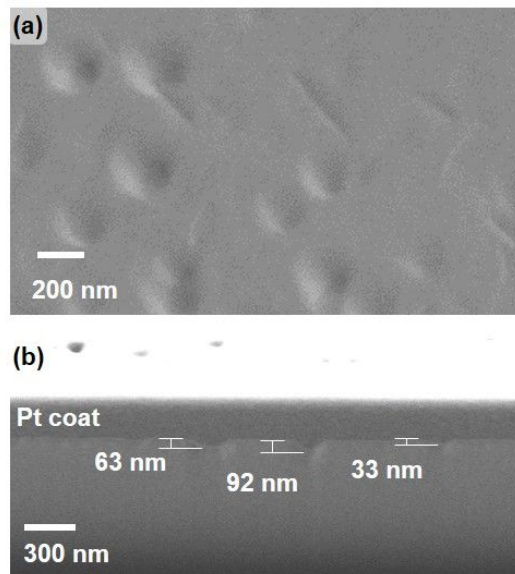


Figure 5.7 (a) Surface and (b) cross sectional SEM images of deuterium ion-irradiated PW-h targets which are pre-damaged by heat flux irradiation with $T = 1705\text{ }^{\circ}\text{C}$, 4.2 MW/m^2 , 800 s

5.2 Damage aggravation of ion pre-irradiated tungsten by heat flux irradiation

5.2.1 Heat-flux irradiation on blister reach surface of tungsten

To examine the aggravation of pre-generated blisters, heat-flux irradiation of an ion pre-irradiated tungsten surface was conducted. Two target types (vertically elongated (KW-v) and horizontally elongated (PW-h)) were first ion-irradiated and blister reach surfaces were obtained under 50 – 200 eV impact energy and 30 – 60 min irradiation time. All ion-irradiated tungsten targets were confirmed to have three kinds of fully developed blisters by SEM analysis. The blister reach surfaces of the tungsten targets were further irradiated by a heat flux of approximately 5MW/m² with a surface temperature of 1,700 °C and irradiation time of 400 s. The full irradiation conditions are given in Table 5.2. After the heat-flux irradiation, the target surfaces were completely recrystallized. The variations in the pre-generated blisters were examined through image analysis using FE-SEM imaging and FIB cross sectioning

Table 5.2 Conditions of pre-ion irradiation and aggravation by heat flux irradiation

Type	Ion flux irradiation		Heat flux irradiation		
	Incident energy [eV]	Fluence [#/m ²]	T _{surface} [°C]	q [MW/m ²]	Irradiation time [s]
KW-v	50 - 200	~ 10 ²⁴	1700	4 - 5	50 - 400
PW-h	50 - 200	~ 10 ²⁴	1700	4 - 5	50 - 400

5.2.2 Characteristics of aggravated damage of ion pre-irradiated tungsten by heat-flux irradiation

The heat-flux irradiation was conducted on the surface of the deuterium-ion pre-irradiated tungsten targets. The high-temperature environment induced by the heat flux caused aggravation of the blisters and full recrystallization of the target surfaces. The three types of generated blisters exhibited different shape variations after the heat-flux irradiation, due to differences in the size, thickness, and quantity of contained gas. The small dome-shaped blisters, which were the smallest and thinnest of the blisters, were thermally burst and fully eradicated by the atomic diffusion, as shown in Figure 5.8. Only dented traces remained after the heat-flux irradiation. This vanishing of the small dome-shaped blisters occurred evenly on the KW-v and PW-h target surfaces. The medium terrace-shaped blisters, which occurred only on the surface of the PW-h target were altered dramatically, displaying the increased size and thermal bursting shown in Figure 5.9. The medium terrace-shaped blisters had underlying cavities originating from grain boundary cracks and slips within the grains, as discussed in section 4.3.1. These cavities were expanded depending on the nearby grain boundaries. This was due to increased internal gas pressure in the elevated-temperature environment. The expansion of the underlying cavities continued to the moment of thermal bursting. The roofs of the expanded blisters were not recrystallized with underlying bulk grains and remained separate from the bulk body with many small grains. These roofs could be thermal barriers that caused abnormal local overheating of the target. The large irregular-shaped blisters had identical characteristics to the medium terrace-shaped blisters, as can be seen in Figure 5.10. Cavity expansion and thermal bursting were also the main damage aggravation mechanisms of the large irregular-shaped blisters.

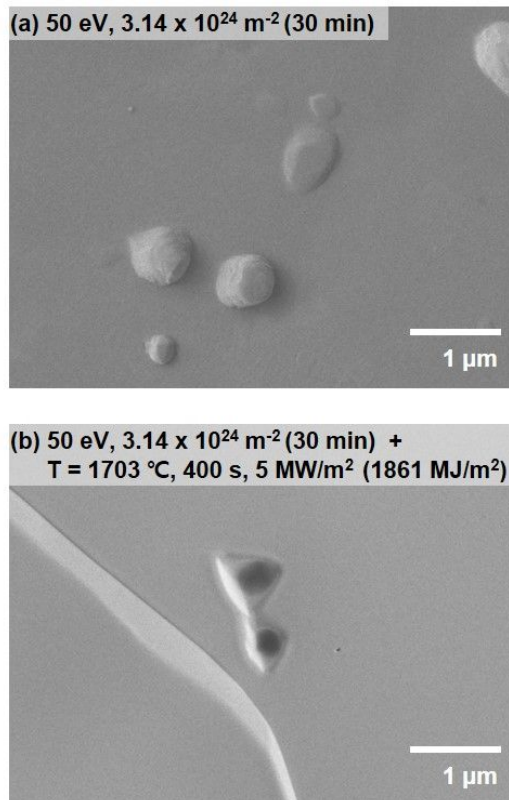


Figure 5.8 SEM images for aggravation of small dome-shaped blister by heat flux irradiation

(a) deuterium ion-irradiated surface with conditions of 50 eV, $3.14 \times 10^{24} \text{ m}^{-2}$ (30 min)

(b) additional heat flux irradiation with conditions of $T = 1703 \text{ }^\circ\text{C}$, 400 s, 5 MW/m^2 (1861 MJ/m^2)

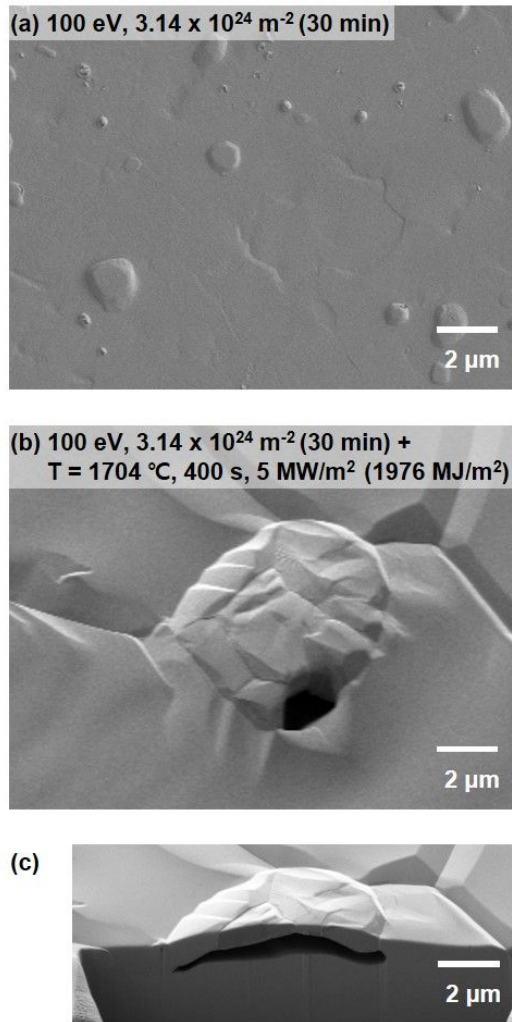


Figure 5.9 SEM images for aggravation of medium dome-shaped blister by heat flux irradiation

(a) deuterium ion-irradiated surface with conditions of 100 eV, $3.14 \times 10^{24} \text{ m}^{-2}$ (30 min)

(b) additional heat flux irradiation with conditions of $T = 1704 \text{ }^\circ\text{C}$, 400 s, 5 MW/m^2 (1976 MJ/m^2)

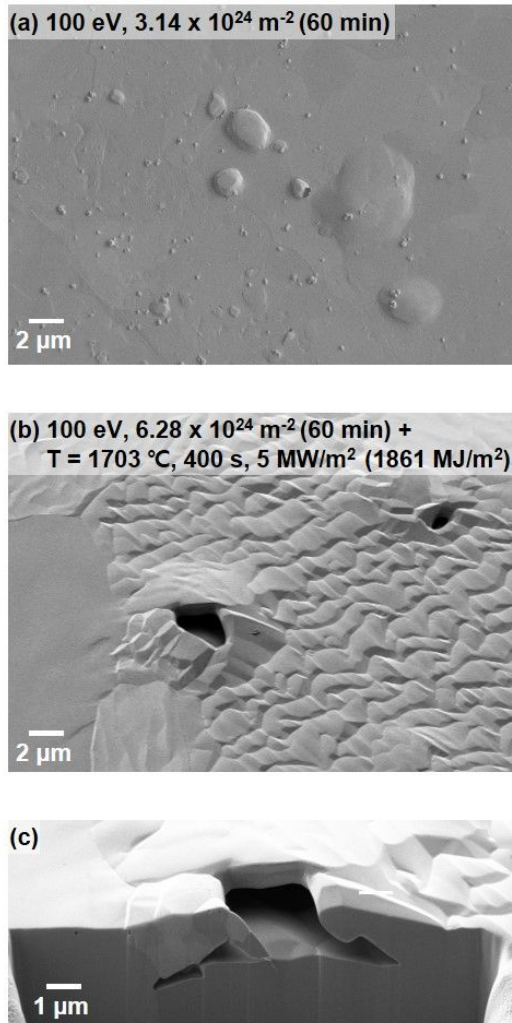


Figure 5.10 SEM images for aggravation of large irregular-shaped blister by heat flux irradiation

(a) deuterium ion-irradiated surface with conditions of 100 eV, $6.28 \times 10^{24} \text{ m}^{-2}$ (60 min)

(b) additional heat flux irradiation with conditions of $T = 1703 \text{ }^\circ\text{C}$, 400 s, 5 MW/m^2 (1861 MJ/m^2)

Chapter 6

Conclusion

In this dissertation, the damage mechanisms operating on a tungsten surface are studied using heat-flux irradiation and deuterium-ion irradiation under nuclear-fusion-plasma-relevant conditions. The surface damage caused by both thermal and particle effects are analyzed separately in order to develop an understanding of the characteristics of tungsten in a high heat-flux environment under high-temperature and high particle-flux conditions, respectively. To examine the complex effects of thermal and particle irradiation, the resultant damage aggravation is discussed for additional particle and thermal irradiation on thermally pre-irradiated and particle pre-irradiated tungsten targets, respectively. All the irradiation is conducted on targets with different grain structures, i.e., vertically and horizontally elongated grains. From these results, the damage sustained by the tungsten surface is discussed with regard to the material characteristics as well as the plasma-facing conditions.

Tungsten as a metal plasma facing material (PFM) is significantly affected by temperature. Under the influence of a sufficiently high temperature, tungsten demonstrates significant variation in its grain structure, e.g., recrystallization. Recrystallized tungsten exhibits an enlarged grain and a specific thickness saturation. The initial grain elongation direction is a critical factor determining the characteristics of the internal damage within the recrystallization layer. The recrystallized KW-v sample exhibits a large amount of sub-grains and internal cracks only, which occurred at sub-grain boundaries, while the recrystallized PW-h has no internal cracks.

The damage caused by ion irradiation, known as blisters, is classified into three types depending on size and shape of the blisters. The smallest blister type has a dome shape with a thicker top and thinner side wall. The medium-sized blister has a terraced shape with a flat top and stiffly inclined side wall, while the largest blister has no specific shape and exhibits irregular changes and a moderately swollen shape. The medium terrace-shaped and large irregular-shaped blisters have greater thickness than the small dome-shaped blisters, because they begin at grain boundaries beneath the surface. With increased fluence, the blisters exhibit increased size and number density, that is, apart from the medium terrace-shaped blister. All of the blisters exhibit a tendency towards increased size and decreased number density in response to increased deuterium-ion incident energy. The generated blisters are eradicated under high-incident energy and large deuterium-ion fluence conditions. As can be prominently seen in the case of the small dome-shaped blister, a key factor in blister destruction is the local incident angle of the increased sputtering, which causes blister bursting at the blister side wall. The destruction of blisters by a sputtering-aided burst is also apparent in the case of the medium terrace-shaped blister, which has a side wall that satisfies the required incident angle condition for maximum sputtering. In contrast, since this incident angle requirement is not met by the large irregular-shaped blister surface, the destruction of large blisters does not occur. In the case of high incident energy and large fluence, the small dome-shape blister is completely destroyed with full bursting, while the medium terrace shaped blister is partially destroyed and experiences side wall bursting. No destruction of the large irregular-shaped blister occurs. Therefore, the tungsten surface that has a vertically elongated grain is vulnerable to particle-driven damage generation, because only small dome-shaped

blisters occur in large numbers on this target surface.

For damage aggravation of the tungsten surface, additional irradiation of thermally pre-irradiated and ion pre-irradiated tungsten targets is conducted using deuterium-ion and heat flux, respectively. The ion irradiation on the heat-flux-irradiated surface increases the pre-generated internal target damage significantly. Sub-grains that exist in the recrystallized KW-v target and have bubbles and cracks at the sub-grain boundaries are ejected by accumulated deuterium gas pressure at the boundary cracks. This sub-grain ejection is the largest particle influx into the plasma, but this ejection occurs very rarely. Hence, the total number of ejected tungsten atoms is not sufficiently high to affect the facing plasma. The recrystallized PW-h target shows no noticeable damage within the target. However, after deuterium-ion irradiation, the target surface exhibits large holes that originate from hydrogen bubbling at near-surface defects. A single hole is relatively smaller than an ejected sub-grain. However, hole generation occurs very frequently. Therefore, a larger number of tungsten atoms is emitted by hole generation than by sub-grain ejection. Hence, the target with a vertically elongated grain is advantageous for use with high-temperature plasma and frequent additional particle-irradiation scenarios.

The additional heat-flux irradiation of the ion pre-irradiated tungsten destroys the blisters through thermal bursting. The small dome-shaped blister is completely destroyed by blister thermal bursting, leaving only a small dent on the target surface. The medium terrace-shaped and large irregular-shaped blisters, which are generated on the horizontally elongated grain surface only, expand toward the underlying grain boundaries and thermally burst, while retaining the blister structure. These remaining bubble components exhibit larger areas than the burst area and function as a thermal

barrier.

In the heat-flux dominant condition, the vertically elongated grain causes internal damage such as cracks, which are the seeds of sub-grain ejection. Sub-grain ejection occurs less frequently than hole-structure generation, which is a quite frequent occurrence on recrystallized targets with horizontally elongated grains. In other words, it can be deduced that internal cracks at sub-grain boundaries prevent greater erosion by hole structure generation. Therefore, tungsten that has a vertically elongated grain is advantageous in heat-flux-dominant plasma scenarios.

As regards the deuterium-ion-dominant condition, the vertically elongated grain causes small dome-shaped blisters only, while horizontally elongated grains induce all blister types with remarkably reduced blister number density. Because the small dome-shaped blisters are completely destroyed by sputtering-aided and thermal-aided bursts, tungsten with a vertically elongated grain is eroded significantly under particle-dominant conditions. Therefore, tungsten with horizontally elongated grains has an advantage in particle-dominant conditions, because of the lower number density of the small dome-shaped blisters.

Form the results obtained in this study, the damage mechanisms affecting a tungsten surface can be understood through consideration of the plasma conditions and material characteristics. For the minimization of surface damages and related erosion, the tungsten type can be suggested to the first wall and divertor materials as tungsten with horizontally elongated and vertically elongated, respectively. In addition, it is firstly proved that the defects in nano or micrometer scale are origins of surface damages and revealed by the irradiations of high heat flux and deuterium ions. Therefore, to reduce surface damages of tungsten PFMs, the defects have to be

controlled at a manufacturing process. Further quantitative analysis of this damage generation and defects characteristics will provides a baseline data for the development of highly plasma resistant PFMs and a selection of proper material to each plasma condition.

Bibliography

- [1] J. Wesson, *Tokamaks*, Third edit. New York: Oxford University Press, 2004, p.3.
- [2] G. Federici, "Plasma wall interactions in ITER," *Phys. Scr.*, vol. T124, pp.1–8, 2006.
- [3] J. M. Linke, T. Hirai, M. Rödiger, and L. A. Singheiser, "Performance of plasma-facing materials under intense thermal loads in tokamaks and stellarators," *Fusion Sci. Technol.*, vol. 46, pp.142–151, 2004.
- [4] J. W. Davis and P. D. Smith, "ITER material properties handbook," *J. Nucl. Mater.*, vol. 233–237, pp.1593–1596, 1996.
- [5] V. Barabash, M. Akiba, J. P. Bonal, G. Federici, R. Matera, K. Nakamura, H. D. Pacher, M. Rödiger, G. Vieider, and C. H. Wu, "Carbon fiber composites application in ITER plasma facing components," *J. Nucl. Mater.*, vol. 258–263, pp.149–159, 1998.
- [6] L. Singheiser, T. Hirai, J. Linke, G. Pintsuk, and M. Rödiger, "Plasma-facing materials for thermo-nuclear fusion devices," *Trans. Indian Inst. Met.*, vol. 62, pp.123–128, 2009.

- [7] T. Pütterich, R. Neu, R. Dux, A. D. Whiteford, M. G. O'Mullane, and H. P. Summers, "Calculation and experimental test of the cooling factor of tungsten," *Nucl. Fusion*, vol. 50, 025012, 2010.
- [8] V. Philipps, "Tungsten as material for plasma-facing components in fusion devices," *J. Nucl. Mater.*, vol. 415, pp.S2–S9, 2011.
- [9] R. Behrisch, G. Federici, A. Kukushkin, and D. Reiter, "Material erosion at the vessel walls of future fusion devices," *J. Nucl. Mater.*, vol. 313–316, pp.388–392, 2003.
- [10] J. Roth, E. Tsitrone, A. Loarte, T. Loarer, G. Counsell, R. Neu, V. Philipps, S. Brezinsek, M. Lehnen, P. Coad, C. Grisolia, K. Schmid, K. Krieger, A. Kallenbach, B. Lipschultz, R. Doerner, R. Causey, V. Alimov, W. Shu, O. Ogorodnikova, A. Kirschner, G. Federici, and A. Kukushkin, "Recent analysis of key plasma wall interactions issues for ITER," *J. Nucl. Mater.*, vol. 390–391, pp.1–9, 2009.
- [11] T. Tanabe, "Tritium issues to be solved for establishment of a fusion reactor," *Fusion Eng. Des.*, vol. 87, pp.722–727, 2012.
- [12] Erik Lassner and Wolf-Dieter Schubert, *Tungsten : Properties, Chemistry, Technology of the Element, Alloys, and Chemical Compounds*. New York: Kluwer Academic / Plenum Publishers, 1999.
- [13] J. Linke, M. Akiba, H. Bolt, G. Breitbach, R. Duwe, A. Makhankov, I. Ovchinnikov, M. Rödiger, and E. Wallura, "Performance of beryllium, carbon,

- and tungsten under intense thermal fluxes,” *J. Nucl. Mater.*, vol. 241–243, pp.1210–1216, 1997.
- [14] V. Barabash, M. Akiba, I. Mazul, M. Ulrickson, and G. Vieider, “Selection, development and characterisation of plasma facing materials for ITER,” *J. Nucl. Mater.*, vol. 233–237, pp.718–723, 1996.
- [15] M. Merola, G. Vieider, M. Bet, I. Bobin Vastra, L. Briottet, P. Chappuis, K. Cheyne, G. Dell’Orco, D. Duglué, R. Duwe, S. Erskine, F. Escourbiac, M. Febvre, M. Grattarola, F. Moreschi, A. Orsini, R. Pamato, L. Petrizzi, L. Plöchl, B. Riccardi, E. Rigal, M. Rödig, J. . Salavy, B. Schedler, J. Schlosser, S. Tähtinen, R. Vesprini, E. Visca, and C. . Wu, “European achievements for ITER high heat flux components,” *Fusion Eng. Des.*, vol. 56–57, pp.173–178, 2001.
- [16] G. Federici, H. Wuerz, G. Janeschitz, and R. Tivey, “Erosion of plasma-facing components in ITER,” *Fusion Eng. Des.*, vol. 61–62, pp.81–94, 2002.
- [17] O. M. Wirtz, *Thermal Shock Behaviour of Different Tungsten Grades under Varying Conditions*. Jülich: Forschungszentrum Jülich GmbH, 2012.
- [18] D. N. Hill, “A review of elms in divertor tokamaks,” *J. Nucl. Mater.*, vol. 241–243, pp.182–198, 1997.
- [19] M. Becoulet, G. Huysmans, P. Thomas, E. Joffrin, F. Rimini, P. Monier-Garbet, A. Grosman, P. Ghendrih, V. Parail, P. Lomas, G. Matthews, H. Wilson, M. Gryaznevich, G. Counsell, A. Loarte, G. Saibene, R. Sartori, A. Leonard, P.

- Snyder, T. Evans, P. Gohil, R. Moyer, Y. Kamada, N. Oyama, T. Hatae, K. Kamiya, A. Degeling, Y. Martin, J. Lister, J. Rapp, C. Perez, P. Lang, A. Chankin, T. Eich, A. Sips, J. Stober, L. Horton, A. Kallenbach, W. Suttrop, S. Saarelma, S. Cowley, J. Lönnroth, M. Shimada, A. Polevoi, and G. Federici, “Edge localized modes control: experiment and theory,” *J. Nucl. Mater.*, vol. 337–339, pp.677–683, 2005.
- [20] J. Linke, P. Lorenzetto, P. Majerus, M. Merola, D. Pitzer, and M. Rödiger, “EU development of high heat flux components,” *Fusion Sci. Technol.*, vol. 47, pp.678–685, 2005.
- [21] O. Gruber, K. Lackner, G. Pautasso, U. Seidel, and B. Streibl, “Vertical displacement events and halo currents,” *Plasma Phys. Control. Fusion*, vol. 35, pp.B191–B204, 1993.
- [22] A. Hassanein, T. Sizyuk, and M. Ulrickson, “Vertical displacement events: A serious concern in future ITER operation,” *Fusion Eng. Des.*, vol. 83, pp.1020–1024, 2008.
- [23] B. Lipschultz, J. W. Coenen, H. S. Barnard, N. T. Howard, M. L. Reinke, D. G. Whyte, and G. M. Wright, “Divertor tungsten tile melting and its effect on core plasma performance,” *Nucl. Fusion*, vol. 52, 123002, 2012.
- [24] J. W. Coenen, V. Philipps, S. Brezinsek, G. Pintsuk, I. Uytendhouwen, M. Wirtz, A. Kreter, K. Sugiyama, H. Kurishita, Y. Torikai, Y. Ueda, and U. Samm, “Melt-layer ejection and material changes of three different tungsten

- materials under high heat-flux conditions in the tokamak edge plasma of TEXTOR,” *Nucl. Fusion*, vol. 51, 113020, 2011.
- [25] I. E. Garkusha, N. N. Aksenov, A. A. Chuvilo, I. S. Landman, V. A. Makhraj, S. V Malykhin, A. T. Pugachev, M. J. Sadowski, and E. Skladnik-Sadowska, “Transient plasma loads to the ITER divertor surfaces: Simulation experiments with QSPA Kh-50,” *Nukleonika*, vol. 57, pp.167–170, 2011.
- [26] T. Loewenhoff, J. Linke, G. Pintsuk, and C. Thomser, “Tungsten and CFC degradation under combined high cycle transient and steady state heat loads,” *Fusion Eng. Des.*, vol. 87, pp.1201–1205, 2012.
- [27] J. W. Coenen, B. Bazylev, S. Brezinsek, V. Philipps, T. Hirai, A. Kreter, J. Linke, G. Pintsuk, G. Sergienko, A. Pospieszczyk, T. Tanabe, Y. Ueda, and U. Samm, “Material and power-handling properties of tungsten PFCs after steady-state melting and additional transient high-heat-flux exposure,” *Fusion Sci. Technol.*, vol. 61, pp.129–135, 2012.
- [28] N. S. Klimov, V. L. Podkovyrov, D. V Kovalenko, A. M. Zhitlukhin, V. A. Barsuk, I. V Mazul, R. N. Giniyatulin, V. Y. Kuznetsov, B. Riccardi, A. Loarte, M. Merola, V. S. Koidan, J. Linke, I. S. Landman, S. E. Pestchanyi, and B. N. Bazylev, “Experimental study of divertor plasma-facing components damage under a combination of pulsed and quasi-stationary heat loads relevant to expected transient events at ITER,” *Phys. Scr.*, vol. T145, 014064, 2011.

- [29] T. Loewenhoff, A. Bürger, J. Linke, G. Pintsuk, A. Schmidt, L. Singheiser, and C. Thomser, “Evolution of tungsten degradation under combined high cycle edge-localized mode and steady-state heat loads,” *Phys. Scr.*, vol. T145, 014057, 2011.
- [30] M. Wirtz, J. Linke, G. Pintsuk, L. Singheiser, and I. Uytendhouwen, “Comparison of the thermal shock performance of different tungsten grades and the influence of microstructure on the damage behaviour,” *Phys. Scr.*, vol. T145, 014058, 2011.
- [31] G. Pintsuk, A. Prokhotseva, and I. Uytendhouwen, “Thermal shock characterization of tungsten deformed in two orthogonal directions,” *J. Nucl. Mater.*, vol. 417, pp.481–486, 2011.
- [32] S. Pestchanyi, I. Garkusha, and I. Landman, “Simulation of tungsten armour cracking due to small ELMs in ITER,” *Fusion Eng. Des.*, vol. 85, pp.1697–1701, 2010.
- [33] V. A. Makhraj, I. E. Garkusha, N. N. Aksenov, N. V Kulik, I. S. Landman, J. Linke, A. V Medvedev, S. V Malykhin, V. V Chebotarev, A. T. Pugachev, and V. I. Tereshin, “High heat flux plasma testing of iter divertor materials under elm relevant conditions in qspa kh-50,” *Probl. At. Sci. Technol.*, pp.57–59, 2010.
- [34] I. E. Garkusha, A. N. Bandura, O. V Byrka, V. V Chebotarev, I. Landman, V. A. Makhraj, S. Pestchanyi, and V. I. Tereshin, “Damage to preheated tungsten

- targets after multiple plasma impacts simulating ITER ELMs,” *J. Nucl. Mater.*, vol. 386–388, pp.127–131, 2009.
- [35] T. Zhang, Y. Wang, Y. Zhou, T. Lei, and G. Song, “Model to determine recrystallization temperature of tungsten based dilute solid solution alloys,” *J. Mater. Sci.*, vol. 41, pp.7506–7508, 2006.
- [36] F. J. Humphreys and M. Hatherly, *Recrystallization and Related Annealing Phenomena*. Oxford: Elsevier, 2004.
- [37] Y. Yuan, H. Greuner, B. Böswirth, K. Krieger, G.-N. Luo, H. Y. Xu, B. Q. Fu, M. Li, and W. Liu, “Recrystallization and grain growth behavior of rolled tungsten under VDE-like short pulse high heat flux loads,” *J. Nucl. Mater.*, vol. 433, pp.523–530, 2013.
- [38] Y. Ueda, J. W. Coenen, G. De Temmerman, R. P. Doerner, J. Linke, V. Philipps, and E. Tsitrone, “Research status and issues of tungsten plasma facing materials for ITER and beyond,” *Fusion Eng. Des.*, vol. 89, pp.901–906, 2014.
- [39] S. Lindig, M. Balden, V. K. Alimov, T. Yamanishi, W. M. Shu, and J. Roth, “Subsurface morphology changes due to deuterium bombardment of tungsten,” *Phys. Scr.*, vol. T138, 14040, 2009.
- [40] V. K. Alimov, W. M. Shu, J. Roth, K. Sugiyama, S. Lindig, M. Balden, K. Isobe, and T. Yamanishi, “Surface morphology and deuterium retention in tungsten exposed to low-energy, high flux pure and helium-seeded deuterium plasmas,” *Phys. Scr.*, vol. T138, 14048, 2009.

- [41] R. D. Kolasinski, M. Shimada, D. A. Buchenauer, R. A. Causey, T. Otsuka, W. M. Clift, J. M. Shea, T. R. Allen, P. Calderoni, and J. P. Sharpe, “Characterization of surface morphology and retention in tungsten materials exposed to high fluxes of deuterium ions in the tritium plasma experiment,” *Phys. Scr. T*, vol. T138, 14042, 2009.
- [42] M. Miyamoto, D. Nishijima, M. J. Baldwin, R. P. Doerner, Y. Ueda, K. Yasunaga, N. Yoshida, and K. Ono, “Microscopic damage of tungsten exposed to deuterium-helium mixture plasma in PISCES and its impacts on retention property,” *J. Nucl. Mater.*, vol. 415, pp.S657–S660, 2011.
- [43] P. E. Lhuillier, T. Belhabib, P. Desgardin, B. Courtois, T. Sauvage, M. F. Barthe, A. L. Thomann, P. Brault, and Y. Tessier, “Helium retention and early stages of helium-vacancy complexes formation in low energy helium-implanted tungsten,” *J. Nucl. Mater.*, vol. 433, pp.305–313, 2013.
- [44] S. I. Krasheninnikov and R. D. Smirnov, “On ‘bubbly’ structures in plasma facing components,” *J. Nucl. Mater.*, vol. 438, pp.S861–S864, 2013.
- [45] W. . Shu, E. Wakai, and T. Yamanishi, “Blister bursting and deuterium bursting release from tungsten exposed to high fluences of high flux and low energy deuterium plasma,” *Nucl. Fusion*, vol. 47, pp.201–209, 2007.
- [46] K. Tokunaga, M. J. Baldwin, R. P. Doerner, N. Noda, Y. Kubota, N. Yoshida, T. Sogabe, T. Kato, and B. Schedler, “Blister formation and deuterium retention

- on tungsten exposed to low energy and high flux deuterium plasma,” *J. Nucl. Mater.*, vol. 337–339, pp.887–891, 2005.
- [47] W. M. Shu, “High-dome blisters formed by deuterium-induced local superplasticity,” *Appl. Phys. Lett.*, vol. 92, 211904, 2008.
- [48] W. M. Shu, A. Kawasuso, and T. Yamanishi, “Recent findings on blistering and deuterium retention in tungsten exposed to high-fluence deuterium plasma,” *J. Nucl. Mater.*, vol. 386–388, pp.356–359, 2009.
- [49] S. H. Hong, *Optimal Design and Fabrication Technology of Thermal Plasma Torches for Industrial Application*. Seoul: Seoul National University, 2005.
- [50] R. Zorat and D. Vender, “Global model for an rf hydrogen inductive plasma discharge in the deuterium negative ion source experiment including negative ions,” *J. Phys. D. Appl. Phys.*, vol. 33, pp.1728–1735, 2000.
- [51] Sung-Ryul Huh, N.-K. Kim, B.-K. Jung, Y.-S. H. Kyoung-Jae Chung, and Gon-Ho Kim, “Global model analysis of negative ion generation in low-pressure hydrogen inductively coupled plasmas with bi-Maxwellian electron energy distributions,” *Phys. Plasmas*, Submitted.
- [52] J. G. Bak, Y. S. Oh, H. S. Kim, S. H. Hahn, S. W. Yoon, Y. M. Jeon, W. W. Xiao, W. H. Ko, W. C. Kim, J. G. Kwak, H. J. Woo, and K. S. Chung, “Electric Probe Measurements at Edge Region During H-Mode Discharges in KSTAR,” *Contrib. to Plasma Phys.*, vol. 53, pp.69–74, 2013.

- [53] D. J. Allen, "Thermal Grooving at migrating grain boundaries," *Scr. Metall.*, vol. 16, pp.5–9, 1982.
- [54] W. W. Mullins, "The effect of thermal grooving on grain boundary motion," *Acta Metall.*, vol. 6, pp.414–427, 1958.
- [55] A. A. Haasz, J. W. Davis, M. Poon, and R. G. Macaulay-Newcombe, "Deuterium retention in tungsten for fusion use," *J. Nucl. Mater.*, vol. 258–263, pp.889–895, 1998.
- [56] T. Ono, M. Ono, K. Shibata, T. Kenmotsu, Z. Li, and T. Kawamura, "Calculation of Sputtering Yield with Obliquely Incident Light-ions (H⁺, D⁺, T⁺, He⁺) and Its Representation by an Extended Semi-empirical Formula," *Res. Rep. NIFS-DATA Series*, vol. 114, pp.1–26, 2012.
- [57] R. Sakamoto, T. Muroga, and N. Yoshida, "Microstructural evolution induced by low energy hydrogen ion irradiation in tungsten," *J. Nucl. Mater.*, vol. 220–222, pp.819–822, 1995.

초 록

핵융합 플라즈마의 차세대 대면 물질로 각광 받고 있는 텅스텐에 대하여 고 열 속 및 중수소 이온 조사에 의해 발생하는 표면 손상의 거동에 대한 연구를 수행하였다. 핵융합 플라즈마에 상응하는 열 속 및 중수소 이온 조사를 위하여 공동형 열 플라즈마 토치를 열원으로, 전자 사이클로 트론 공명 플라즈마를 중수소 이온 원으로 사용한 조사 장치를 개발하여 텅스텐 표면 손상 연구에 적용하였다. 텅스텐 시편은 수직 배열된 결정 구조와 수평 배열된 결정 구조를 가진 두 종류를 사용하여, 재료 특성 차이에 의한 텅스텐 표면의 손상 특성 변화를 고려하였다.

고 열 속 조사에 의하여 텅스텐은 재결정화가 발생하여, 결정의 크기 증가와 함께 한정된 재결정화 두께를 가지는 특성을 보인다. 열 속에 의해 형성된 시편 내부의 수직방향 온도 구배는 텅스텐 내부의 결함이 이동하기 쉬운 환경을 제공하며, 이는 수직 배열된 텅스텐 시편에서 두드러지게 나타나 표면 근방의 아결정립의 경계에 결함이 집속 되어 균열 및 미세 공동이 형성된다. 수평 배열된 텅스텐 시편은 아 결정립 및 내부 균열과 공동 등의 손상은 생성되지 않는 특성을 보였다.

중수소 이온조사는 텅스텐 표면에 3종류의 물질 구조를 형성하였으며, 이는 각각 소형, 중형 및 대형의 물질구조로 구분된다. 소형 물질은 반구형의 구조를 가지며 그 두께가 가장 얇아 스퍼터링에 취약한 형태이다. 특히 측면의 경계로 입사하는 이온은 표면과 약 70° 의 입사각도를 가지는 데, 이는 스퍼터링이 최대화 되는 각도이다. 이러한 각도 효과로 인하여 측면의 스퍼터링이 증가하고, 반구형의 소형 물질 구조는 그 측면이

터지면서 파괴가 시작되어 결국 전체 물질구조가 사라지는 특성을 보인다. 이러한 스퍼터링 증가에 의한 물질구조의 파괴 현상은 테라스 형태의 중형 물질구조에서도 나타나며, 기울어진 측면의 벽이 각도 조건을 만족하여 소형과 같은 측면 터짐 현상이 나타나나, 두꺼운 두께로 인하여 전체의 물질구조의 소멸까지 진행하지 않는다. 불규칙한 구조의 대형 물질은 각도조건을 만족하지 못하여 파괴되지 않는 특성을 보인다.

추가적인 중수소 이온 및 고 열 속 조사를 통하여 손상을 심화 시켰다. 재결정화 된 텅스텐은 추가적인 중이온 조사에 의하여 내부의 결함이 아결정립 분출 및 구멍 구조의 생성으로 표면화 되어 나타난다. 물질 구조는 열 속 조사에 의하여 열 적 파괴 현상이 나타나며, 반구형의 소형 물질은 열에 의한 터짐 현상 및 원자의 확산에 의해 완전히 사라진다. 테라스형태의 중형 및 불규칙한 대형 물질 구조는 열에 의한 결정립 경계의 균열이 확대되어 물질의 크기가 확장되고, 그 이후 국부적 터짐 현상이 발생한다. 남아있는 물질 구조는 열장벽으로 작용하여 고 열 속에 취약한 특성을 나타낸다.

위 결과를 정리하여, 열 속이 주도적인 환경에서 내부수직 배열된 결정 구조를 가지는 텅스텐은 재결정화 및 표면 근방 아결정립 경계의 균열 및 공동 등의 손상을 가진다. 이러한 열 적 손상은 추가적인 중수소 이온 조사 시 아결정립의 분출을 유발한다. 분출되는 아결정립은 매우 적은 회수로 발생하여, 수평 배열된 결정 구조를 가지는 텅스텐 표면에서 발생하는 구멍 구조의 형성에 전체 부식량은 상대적으로 적다. 즉, 아결정립 근방의 균열이 부식이 큰 형태의 손상인 구멍 구조의 형성으로 진행을 막아주는 역할을 한다. 따라서 수직 배열된 결정 구조를 가지는 텅스텐은 열 속의 영향이 주도적인 플라즈마 환경에 적합하다.

입자의 영향이 주가 되는 플라즈마 환경에서, 수직 배열된 결정 구조를 가지는 텅스텐 시편은 돔 형태의 소형 물질구조만 생성되고, 수평 배열된 결정 구조를 가지는 텅스텐 시편은 모든 종류의 물질구조를 가지며, 그 수 밀도는 수직 배열된 결정구조의 텅스텐과 비교하여 매우 작다. 돔 형태의 소형 물질 구조는 스퍼터링 및 열 적 터짐 현상에 의하여 완전히 파괴되어 사라지므로, 수직 배열된 결정 구조를 가지는 텅스텐은 중수소 이온 조사 환경에서는 침식에 매우 취약하다. 따라서 수평 배열된 결정을 가지는 텅스텐은 입자의 영향이 주가 되는 플라즈마 환경에 적합하다.

본 연구 결과를 통하여, 플라즈마 특성 및 대면 재료의 특성에 따른 텅스텐 대면 재료의 손상 거동을 이해하였다. 이를 바탕으로 재료가 가지는 내부 결함에 의하여 대면 재료 표면 손상의 특성이 결정됨을 이해하였다. 이러한 결과를 확장하면, 재료의 결함 이해를 통하여 핵융합로 내벽의 각 위치 별 적합 재료 선정의 기초 자료로 활용될 수 있으며, 나아가 재료의 결함 제어를 통한 고 플라즈마 저항성을 가지는 핵융합로 대면 재료의 개발 방향 제시에 기여할 것으로 기대 된다.

주요어: 플라즈마 표면 상호작용, 텅스텐 대면 재료, 고 열속, 고 입자속, 재결정화, 물질 현상

학 번: 2008-30273

감사의 글

박사과정이라는 긴 시간을 지나, 결실을 맺는 학위논문을 작성하게 되었습니다. 힘들고 어려운 난관이 있었지만, 그만큼 많은 것을 경험하고 배울 수 있는 소중한 시간이었습니다. 무사히 박사 학위를 마칠 수 있게 물심양면으로 도움을 주신 분들께 감사의 인사를 전하고자 합니다.

먼저 학위 과정 동안 큰 가르침을 주신 김곤호 교수님께 감사 드립니다. 교수님께서 몸소 보여주신 학자로서의 지치지 않는 열정을 본받아 박사과정이라는 큰 산을 무사히 넘을 수 있었습니다. 어디서든 교수님의 가르침을 잊지 않도록 끊임없이 노력하겠습니다. 그리고 아낌없는 조언과 관심을 주시고, 바쁘신 와중에도 학위 논문을 심사해 주셨던 황용석 교수님과 백경호 교수님, 한홍남 교수님께 진심으로 감사 드립니다. 또한 관심과 배려로 살피주신 선배님이자, 따뜻한 조언으로 학위논문 심사를 해주신 최수석 교수님께 감사의 인사를 드립니다.

대학원생으로서의 첫 발을 내디디는 부족한 제자에게 큰 가르침을 주시어 이후의 학위 과정에 큰 거름을 주신 존경하는 홍상희 선생님께 깊은 감사의 마음을 전합니다.

지난 박사 과정 동안 좁은 연구실에서 동고동락 해왔던 PAL 여러분들은 평생 잊을 수 없을 것입니다. 특히 같이 졸업하느라 고생한 PAL 6 인방, 연구실 생활이 외롭지 않게 많은 도움을 준 유일한 동기 명선, 연구실 이적 할 때 방장으로 큰 의지가 된 유쾌한 성렬이, 디버터 팀으로 같이 과제하면서 고생한 선택이, 많은 불온(?) 지식을 나누며 사상을 공유한 성영이, 항상 완벽한 준비와 연구 자세로 많은 귀감을 준 설혜, 여러분

들과 졸업을 준비하면서 쌓은 추억은 오래오래 남을 것 같습니다. 그리고 졸업을 위해 물심양면으로 도와준 우리 디버터 팀 후배들, 이제 연구실의 추억으로 앞으로 크게 될 영길이, 다재다능 귀엽고 마음씨 좋은 진영이, 물심양면으로 도와준 연구실 작업 반장 남균이, 나의 일 도와주느라 밤낮 없이 바쁘게 보낸 재민이, 앞으로 고생할 기백이에게 감사 인사 전합니다. 또한 같은 고향 사람으로 많은 의지가 된 현준이, 항상 유쾌한 기운으로 활력을 준 수정이, 잦은 놀림에도 항상 밝은 모습으로 웃음 준 윤창이, 매사가 올바른 상원이, 그리고 늙은 막내 병준이에게 감사의 인사를 전합니다.

마지막으로 언제나 든든한 저의 버팀목이 되어 주시는 사랑하는 가족분들에게 감사 드립니다. 지금은 하늘에 계신 할아버지, 항상 부족한 저를 믿어주신 할머니, 외할머니가 계시기에 힘든 시간을 잘 보낼 수 있었습니다. 항상 사랑으로 대해 주시고, 함께 고생해 주시는 이모님과 친아들처럼 챙겨주시는 고모, 고모부께 감사의 마음을 전합니다. 또한 든든하게 부모님 곁을 지켜 주는 누나와 매형 덕분에 타지에서 학업에 매진할 수 있었습니다. 멀리 떨어진 형 때문에 대신 장손 노릇 하느라 고생한 동생 현민이와 이제 한 가족이 된 제수씨에게 감사의 마음을 전합니다. 한 집에 살면서 친아들처럼 사위를 보살펴 주시고, 언제나 큰 힘을 주시는 장인어른 장모님 그리고 처남 진호에게 감사 드립니다. 부족한 아들을 믿고, 힘든 시기에도 항상 웃음과 사랑으로 보살펴 주시는 아버지 어머님이 계시기에 여기까지 올 수 있었습니다. 더욱 자랑스런 아들이 되기 위해서 부단히 노력하겠습니다. 논문 준비를 핑계로 올빼미처럼 다니는 남편을 믿고 사랑으로 보살펴준 아내 문정에게, 그리고 아빠를 항상 기다려주고

밝은 웃음으로 큰 힘을 주는 아들 동규에게 사랑한다는 말을 전하고 싶습니다.

이 논문을 사랑하는 가족들, 그리고 아들 동규와 아내 문정에게 바칩니다.